

AD-A239 841



2

DTIC
ELECTE
AUG 20 1991
S D

**Efficient, High-Speed, Monolithic Optoelectronic
Circuits Using Quantum-Confined Structures
ARO #DAAL03-89-K-0078 - FINAL REPORT**

04/01/90 - 05/31/91

by

L.A. Coldren: Principal Investigator

J.L. Merz and A.C. Gossard: Associate Investigators

N. Dagli: Faculty Collaborator

J.H. English and D.A. Cohen: Development Engineers

S. W. Corzine, D.B. Young, J.C. Yi and S.-Y. Hu:

Graduate Student Researchers

ECE Technical Report #91-13

This document has been approved
for public release and sale; its
distribution is unlimited.

Department of Electrical & Computer Engineering

University of California at Santa Barbara

July 1991

91-08245



91 8 19 088

REPORT DOCUMENTATION PAGE

Form Approved
OMB No. 0704-0188

Public reporting burden for this collection of information is estimated to average 1 hour per response, including the time for reviewing instructions, searching existing data sources, gathering and maintaining the data needed, and completing and reviewing the collection of information. Send comments regarding this burden estimate or any other aspect of this collection of information, including suggestions for reducing this burden, to Washington Headquarters Services, Directorate for Information Operations and Reports, 1215 Jefferson Davis Highway, Suite 1204, Arlington, VA 22202-4302, and to the Office of Management and Budget, Paperwork Reduction Project (0704-0188), Washington, DC 20503.

1. AGENCY USE ONLY (Leave blank)		2. REPORT DATE 7-25-91		3. REPORT TYPE AND DATES COVERED	
4. TITLE AND SUBTITLE Efficient, High-Speed, Monolithic Optoelectronics Circuits Using Quantum-Confined Structures				5. FUNDING NUMBERS DAAL03-89-K-0078	
6. AUTHOR(S) Larry A. Coldren					
7. PERFORMING ORGANIZATION NAME(S) AND ADDRESS(ES) University of California Dept. of electrical & Computer Engineering Santa Barbara, CA 93106				8. PERFORMING ORGANIZATION REPORT NUMBER	
9. SPONSORING/MONITORING AGENCY NAME(S) AND ADDRESS(ES) U. S. Army Research Office P. O. Box 12211 Research Triangle Park, NC 27709-2211				10. SPONSORING/MONITORING AGENCY REPORT NUMBER ARO 26922.13-EL	
11. SUPPLEMENTARY NOTES The view, opinions and/or findings contained in this report are those of the author(s) and should not be construed as an official Department of the Army position, policy, or decision, unless so designated by other documentation.					
12a. DISTRIBUTION/AVAILABILITY STATEMENT Approved for public release; distribution unlimited.				12b. DISTRIBUTION CODE	
13. ABSTRACT (Maximum 200 words) This is the final report for DAAL03-89-K-0078, a program aimed at developing highly efficient quantum-confined structures for use in optoelectronic circuits using MBE technology. The focus has been primarily on the development of the enabling technologies for high efficiency and speed in integrable diode lasers. Improved MBE growth control for in situ grown quantum-wire structures and the creation of UHV in situ processing techniques have been key technological outcomes of this work. In the device area, one high-risk, high-payoff emphasis has been the growth and analysis of quantum-wire diode lasers. A new growth procedure has been developed for more uniform closely-packed wire arrays. Another device emphasis has been the design and fabrication of highly-efficient vertical-cavity surface-emitting lasers. In this latter area, record device performance has been greatly facilitated by many new theoretical contributions. In this report, we shall attempt to summarize our progress in the materials and processing as well as the device areas.					
14. SUBJECT TERMS Semiconductor lasers, quantum-wire lasers, vertical-cavity surface emitting lasers				15. NUMBER OF PAGES 51	
				16. PRICE CODE	
17. SECURITY CLASSIFICATION OF REPORT UNCLASSIFIED	18. SECURITY CLASSIFICATION OF THIS PAGE UNCLASSIFIED	19. SECURITY CLASSIFICATION OF ABSTRACT UNCLASSIFIED	20. LIMITATION OF ABSTRACT UL		

I. TABLE OF CONTENTS

	Page
II. Introduction and Problem Statement.....	1
III. Molecular Beam Epitaxy -	
Technique improvements for control of quantum wire growth	3
A. Introduction.....	3
B. Quantum Wire Growth	6
IV. <i>In-Situ</i> Processing with MBE.....	9
A. Introduction.....	9
B. Processing Chamber Features and Capabilities.....	10
1. Etch beams and etch processes.....	10
2. Substrate manipulator/stage.....	13
3. Analytical tools	13
4. Gas delivery and vacuum systems.....	14
5. Electron gun purchase	14
C. Summary.....	15
V. Quantum-Well Wire Laser	16
A. Introduction.....	16
B. Layer design and growth.....	17
C. Device fabrication	18
D. Device characterization	20
VI. Theoretical Characteristics of Quantum-Wire Structures.....	22
A. Introduction.....	22
B. TSL Results.....	23
C. SSL Results.....	27
VII. Vertical-Cavity Surface-Emitting Lasers	30
A. Introduction.....	30
B. Calculations.....	30
C. Transversely Pumped Periodic Gain Structure	34
D. Top-to-Bottom Pumped VCSELs.....	36
VIII. Theoretical Gain in Strained and Unstrained Quantum-Well Lasers.....	39
A. Introduction.....	39
B. Calculations.....	40
IX. References.....	49
X. Scientific Personnel	51

II. INTRODUCTION & PROBLEM STATEMENT

This is the final report for DAAL03-89-K-0078, a program aimed at developing highly efficient quantum-confined structures for use in optoelectronic circuits using MBE technology. The focus has been primarily on the development of the enabling technologies for high efficiency and speed in integrable diode lasers, although efficient electro-optic Fabry-Perot modulators have also been explored in the early stages. Improved MBE growth control for *in situ* grown quantum-wire structures and the creation of UHV *in situ* processing techniques have been key technological outcomes of this work. In the device area, one high-risk, high-payoff emphasis has been the growth and analysis of quantum-wire diode lasers. A new growth procedure has been developed for more uniform closely-packed wire arrays. Another device emphasis has been the design and fabrication of highly-efficient vertical-cavity surface-emitting lasers. In this latter area, record device performance has been greatly facilitated by many new theoretical contributions.

In this report, we shall attempt to summarize our progress in the materials and processing as well as the device areas. We begin by reviewing a number of advances in the MBE lab which are primarily directed at improving growth rate control and uniformity so that uniform quantum-wire growth and reproducible vertical-cavity lasers are possible. The next section (Section IV) reviews our progress in developing a UHV *in situ* processing chamber coupled to our MBE system. This should be very instrumental in generating integrated optoelectronic circuits with ultra-small and efficient structures. The basic system is now completely functional and initial calibration results have been encouraging.

Section V outlines a new "serpentine-superlattice" quantum-wire laser, in which the active-layer is more immune to the effects of wire growth inhomogeneities. Initial experimental results show clear quantum-wire effects at low temperature, but with insufficient confinement to operate well at room temperature. Section VI briefly summarizes the results of our theoretical investigations into quantum-wire lasers using either the older tilted superlattices or the new serpentine superlattices. This work is partially sponsored by the NSF Science & Technology Center--QUEST.

Section VII introduces our work on vertical-cavity surface-emitting lasers (VCSELs) which is jointly funded by DARPA. The work supported under this contract has emphasized extensive theoretical design and analysis as well as MBE growth improvements. A very promising device structure that uses lateral contacting of a periodic-gain structure has also been explored. Record results in several areas are reported. The final section (VIII) reviews some of our advances in laser gain theory, which have been the basis of much of the advanced design work on VCSELs. The use of strained-layer quantum-wells has been shown to be especially desirable in both the GaAs and InP materials systems.



Accession For	
NTIS CRASI	J
DTIC TAB	U
Unannounced	U
Justification	
By	
Distribution /	
Availability Codes	
Dist	Avail and/or special
A-1	

III. MOLECULAR BEAM EPITAXY - Technique improvements for control of quantum wire growth

A. Introduction

With the success of quantum well devices in electronics and optoelectronics, research focus has shifted to the next level of confinement, quantum wires. The inclusion of quantum wires in device structures has predicted advantages in speed improvements, threshold reduction (in lasers), as well as other effects. Investigations into the formation of quantum-confined structures such as quantum wires have covered a large number of techniques. The most popular are etching processes, where the quantum structures have confinement provided by etching away some of the grown structure. This technique is limited, as the lithography and etching techniques are difficult to control to the atomic dimensions necessary for good 2-D confinement [1]. Another area under investigation is growth on patterned substrates. This has allowed the formation of quantum wires, but for application to lasers, the wires are oriented in the wrong direction for maximum transition probability [2]. One technique undergoing research at UCSB involves the direct growth of quantum wires on misoriented terraced substrates, the Tilted Superlattice (TSL) growth technique. This technique, which has been described before [3], involves deposition of alternating partial monolayers of GaAs and AlAs on a vicinal substrate, in such a fashion that the GaAs and AlAs layers line up on top of each other as shown in Figure III.1. This can result in a structure with quantum scale confinement in the growth direction as well as perpendicular to the step edges.

The width of the wires, and thus the coupling between them, is determined by both the growth program and the off-axis orientation of the substrate. The main problem with this growth technique is that the growth rates must be known very precisely to make the layers stack up properly. A 1% miscalibration in growth rate will result in a superlattice structure that is angled with respect to the substrate, making thinner and more coupled quantum wires. If the growth rate is off by more than 2%, the angle of the TSL is so high ($\sim 80^\circ$) that the structure is essentially a digital alloy, as the coupling between the wires is very strong. A device structure which minimizes this problem has been under evaluation at UCSB for the last year, and shows great

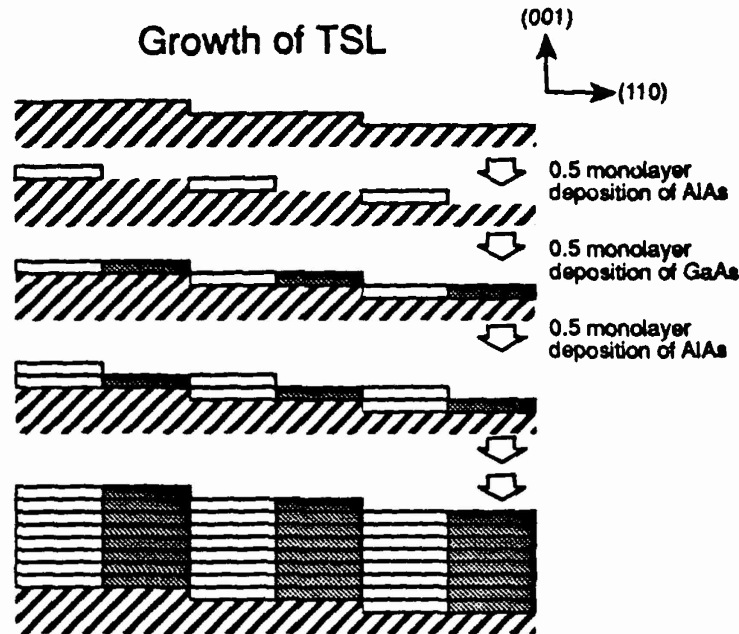


Figure III. 1 Alternating deposition of aluminum arsenide and gallium arsenide partial monolayers results in a tilted superlattice, where the superlattice structure is not normal to the growth direction.

promise. First, however, we should discuss the techniques and improvements made to the MBE system to minimize the uncertainty in the growth rate.

Several issues need to be addressed when growth rate evaluation in MBE is discussed. First, the actual flux control out of the furnaces is an important factor. We have spent a fair amount of time characterizing the flux emission from the growth furnaces. We previously installed a dual-zone gallium furnace in an attempt to reduce oval defect densities and to improve the capacity of the MBE system. This resulted in better uniformity, as the new gallium furnace had a wider mouth than the old system. Unfortunately, this geometry led to a large droop in the gallium flux upon shutter opening, as can be seen in Figure III. 2. Having an accurate knowledge of this droop has helped in the ability to predict layer thicknesses. A new furnace is scheduled to be installed which should decrease the amount of droop in the flux.

The second important issue is the RHEED calibration. Growth rates in MBE are calibrated by measuring the period of the RHEED intensity oscillations. Since the sources are at an angle with respect to the substrate, the growth rate across the sample when not rotated has a significant

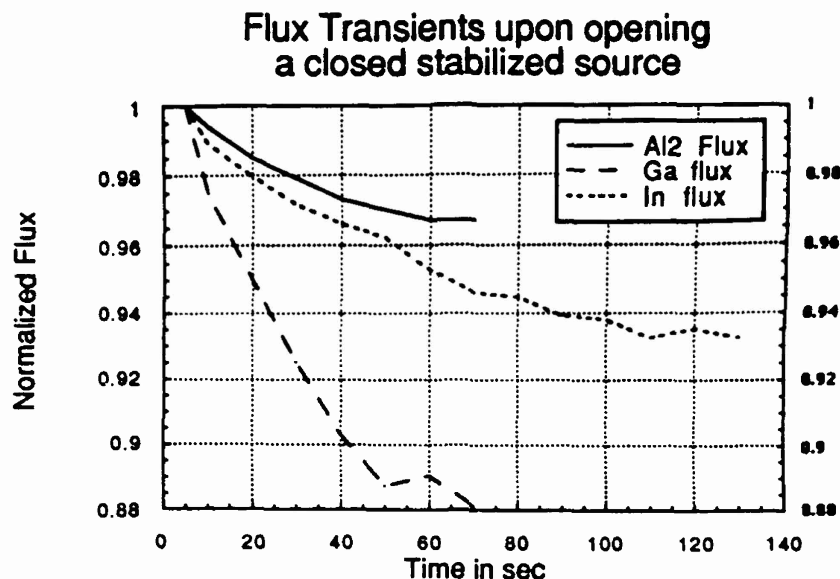


Figure III.2. Group III element fluxes measured starting from shutter opening. Flux drops are minor for the aluminum furnaces, but the gallium furnace exhibits a significant drop in flux after the shutter is opened.

variation, of up to $\pm 15\%$ across a 2" wafer. It is important to have a consistent method of evaluating the growth rate across the wafer when it is either rotated or not rotated. Thus, some other measurement technique is needed. SEM measurements of layer thicknesses are only as good as the calibration of the SEM magnification factor, and can vary according to the conditions under which the measurement is taken. One other technique, related to the Surface Emitting Laser work underway at UCSB, is to use the stop-band of a MBE-grown distributed Bragg reflector (DBR) mirror stack as a calibration tool. The reflectivity spectrum of such a structure is a very sensitive measure of the thickness of the individual layers of the stack, and this can be used to precisely calibrate the growth rates, and to give a calibration factor which can be used with the RHEED oscillations to provide a precise evaluation of the growth rates. This technique allows calibration of the growth rates to within 1%.

The third important factor is the shutter operation. Although the furnace temperature can be controlled relatively accurately, the net growth rate control is only as accurate as the control of the growth furnace shutters. The Varian GEN II system uses AC solenoids to control the shutter operation. These solenoids operate at the zero-crossing of the AC line voltage waveform, and thus

have an accuracy of 1/120th of a second, or 8 milliseconds. At 0.25 micron/hour growth rate, this introduces an uncertainty of 0.006Å for every shutter operation. This may not seem like much, but for TSL work, with shutter operations every 2 seconds, the uncertainty per 1/2 monolayer is around 0.8%, which adds to the meander of the TSL. The control computer currently in use is also a limiting factor, as its time resolution is only 10 ms. This also allows a 1% per 1/2 monolayer uncertainty.

The solution to the solenoid problem is to convert the shutter solenoids and drive electronics to DC operation. This eliminates the random delay encountered with the AC solenoids and has been shown to reduce the uncertainty in the shutter operation to around 1 millisecond. This solution has not yet been implemented, but a detailed design is being developed.

B. Quantum Wire Growth

As mentioned previously, one important area of research at UCSB is in quantum wire formation. Much of the fundamental growth science is supported by the NSF-S&T Center - QUEST. Our approach has been to attempt direct growth of the quantum wires using the TSL technique. This effort is underway because of the advantages inherent in the TSL growth of quantum wires. The ability to make 2-dimensionally confined structures during crystal growth provides much cleaner interfaces than etching techniques are capable of. The dimensions involved are smaller than any lithographic technique yet developed, and the density of wires resulting is much higher than is possible with lithographic techniques. Thus, for example, the density of wires is high enough to allow fabrication of a laser structure with a quantum wire active region oriented perpendicular to the direction of optical propagation. The TSL growth technique has been described above. The efforts underway at UCSB include growth optimization, optical characterization, electrical characterization, and device fabrication. One promising variation of the TSL growth technique is that of the Serpentine Superlattice (SSL), which involves growth of a TSL where the growth rate is swept in small increments around the rate measured by RHEED calibration [4]. This results in a structure with quantum wires in the form of crescents.

Figure III. 3 shows an illustration of this. The advantage this technique has is that the growth rate does not have to be known within 0.1% in order to form quantum wires. The growth rate sweep guarantees that the TSL will be vertical somewhere in the crescent, and thus there will be quantum wires formed. The disadvantage is that the structure is somewhat larger than would be achieved from a standard vertical TSL if the growth rate were known precisely enough to form a vertical TSL. This structure has been grown, and TEM cross-sections as well as polarized photoluminescence measurements have confirmed the presence of the serpentine superlattice and 2-D quantum confinement. Figure III. 4 shows the TEM cross section of the SSL. Polarization dependant photoluminescence measurements were done on this sample, and a strong polarization dependance was observed. Figure III. 5 shows the polarized PL spectrum from one SSL sample. The position of the PL peak suggests that there may be substantial intermixing of the aluminum from the barriers with the wires, so the confinement of these quantum wires is weaker than desired. Work is continuing to identify the aluminum distribution and to improve it.



Figure III.3. Serpentine Superlattice growth. This is a variation on the TSL growth technique intended to reduce the effect of growth rate uncertainty on the quantum wire confinement.



Figure III.4. TEM cross-section showing the Serpentine Superlattice structure. The substrate is a 2° -off vicinal surface, and the barriers are $x=0.5$ composition AlGaAs.

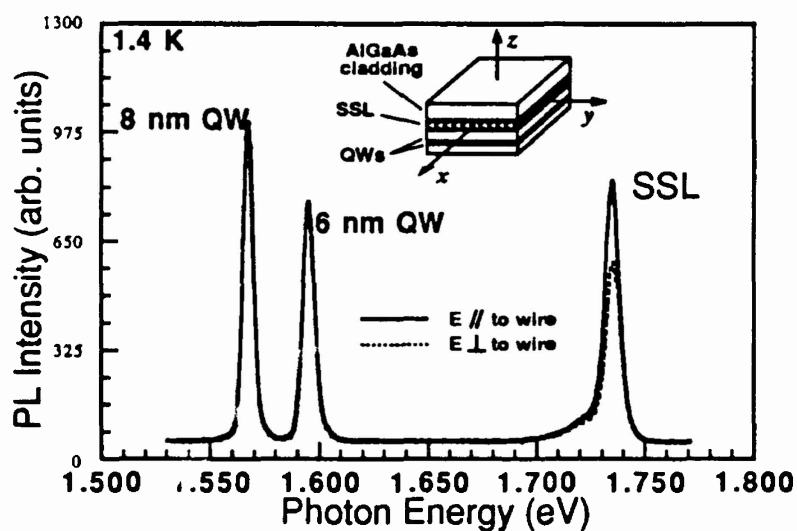


Figure III.5. Polarized Photoluminescence spectra from the Serpentine Superlattice structure. The dashed line shows the PL signal with polarization oriented perpendicular to the quantum wires. The solid line shows the polarization oriented parallel to the wires.

IV. *IN-SITU* PROCESSING WITH MBE

A. Introduction

Fabricating high-quality quantum wire nanostructures requires a low-damage process with high-resolution control of both vertical and lateral dimensions. Our approach is to process epi substrates *in-situ* with our two MBE machines. By never exposing the substrates to atmospheric pressure and contamination, and by using low-damage etch processes that can form patterns without organic resists, we will minimize defects and contamination at MBE regrowth interfaces, and we should expect improvements in the number of useful devices per wafer. With these goals in mind, a UHV processing chamber with multiple etch capabilities has been designed and installed onto the UHV tunnel that connects our two Varian Gen-II MBE machines. In addition, a focussed ion beam (FIB) machine and a UHV scanning tunnelling microscope are accessible via a UHV shuttle. This multichamber *in-situ* processing system is shown in Figure IV. 1. An electron gun is being purchased and will be installed on the processing chamber by the end of this year, for use in pattern generation and imaging (see below). This part of the report will be devoted primarily to the new processing chamber as presently configured.

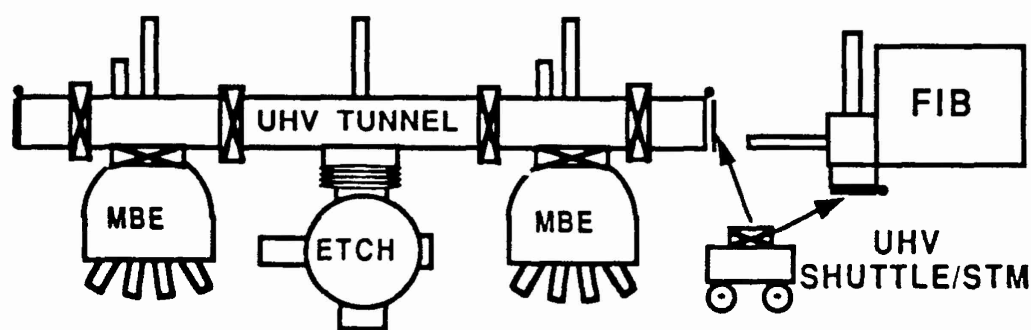


Figure IV. 1. Schematic of multichamber *in-situ* processing system, showing two molecular beam epitaxy (MBE) machines, etch chamber, focussed ion beam (FIB), and scanning tunnelling microscope (inside the UHV shuttle).

B. Processing Chamber Features and Capabilities

1. Etch beams and etch processes

A more detailed representation of the processing chamber is given in Figure IV. 2.. The primary processing features are an argon ion beam and a reactive gas inlet with an inline microwave source capable of cracking the gas to form a "radical beam." These two beams give us independent control of the physical (ion beam) and chemical (gas or radical beam) components of a given etch or surface preclean process. Thus, it included the same Radical-Beam Ion-Beam-Etching (RBIBE) process we have discussed previously [5].

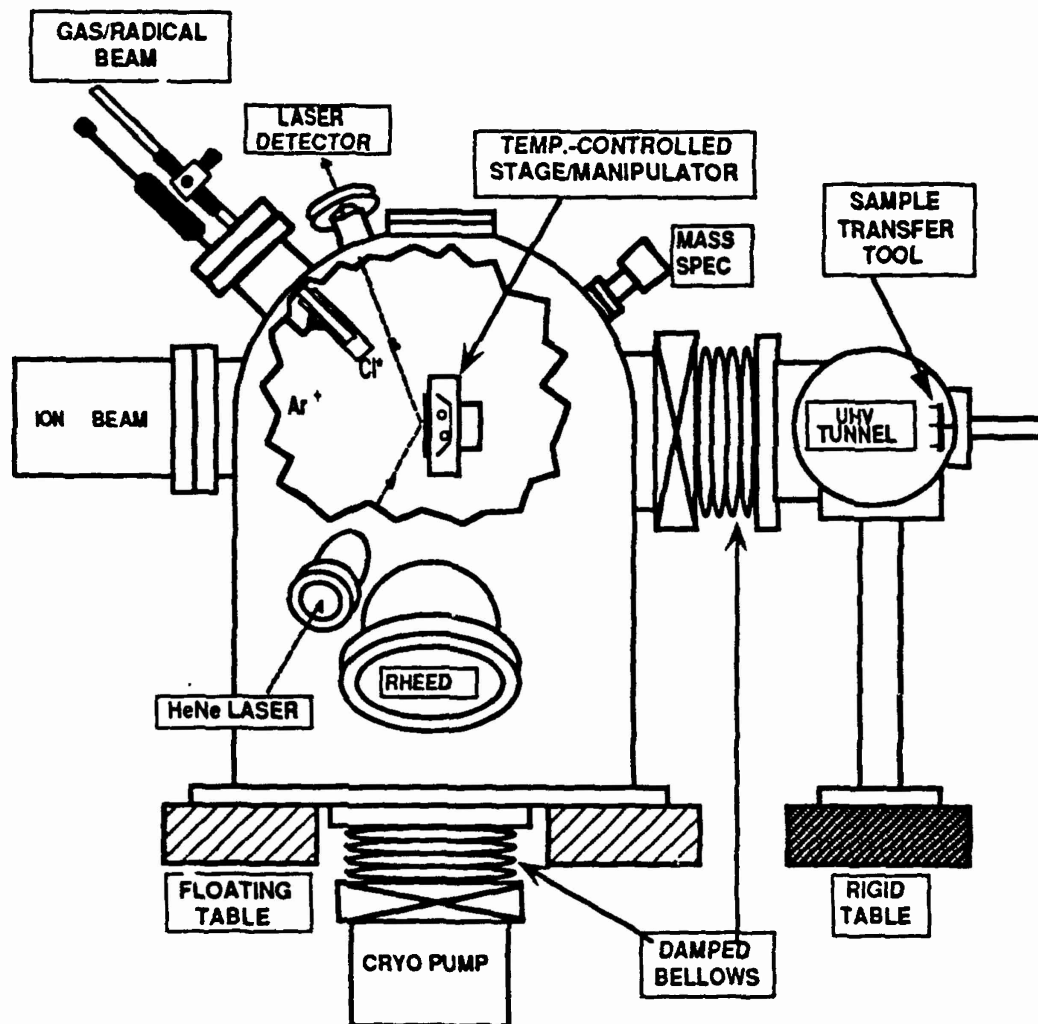


Figure IV. 2. Schematic of in-situ processing chamber, with important components labelled--see text for description.

The ion beam is a 5-cm Kaufman-type source made by Ion Tech, Inc. It has a hollow cathode ion source and a hollow cathode neutralizer for high reliability and low contamination. Argon is heated until a small plasma is formed in the "keeper" sections of the cathode and neutralizer. Electrons are removed from the cathode keeper to ionize the beam gas (reactive or inert). From the neutralizer keeper, electrons are removed near ground potential in a beam that is perpendicular to the ion beam; these electrons couple with the ion beam to yield a net zero current density, eliminating charging problems on our semi-insulating substrates. A Faraday cup built into an MBE substrate holder allows ion beam current density profiling at the same point in space as the substrates. So far, only argon gas has been used as an ion source. Low-damage argon beams with ion energies as low as 75eV can be produced at a total chamber pressure of 0.5 millitorr or less, with 200eV beams being our present standard. Argon ion beam etching (IBE) is a purely physical etch that we will utilize to remove the topmost oxidized or contaminated layers (< 100 angstroms) of a substrate. Further etching is then accomplished (1) by combining the argon ion beam with either a reactive gas beam (ion beam assisted etch, IBAE) or a reactive radical beam (radical beam/ion beam etch, RBIBE), or (2) by turning off the ion beam and etching with only the reactive gas (gas beam etch, GBE) or radical beam (radical beam etch, RBE).

Radical beams are produced via a McCarroll microwave cavity attached around a quartz tube with a quartz "trombone" extender. The extender is used to control the flux of reactive gases or radicals at the substrate surface. An Ophos, Inc. power supply delivers up to 100 forward watts to the air-cooled microwave cavity, and a tesla coil provides the spark necessary to strike the radical plasma. A minimum pressure of about 0.3 millitorr is necessary to maintain a plasma. Three ultra-high purity reactive gases -- chlorine, oxygen, and hydrogen -- are available. Oxygen RBE, followed by hydrogen RBE, will be utilized to remove organic contaminants and surface oxides, respectively, before MBE growth or regrowth. Selective chlorine GBE of GaAs over AlGaAs or AlAs on patterned substrates will be accomplished by forming a chemically-inert aluminum oxide layer with a small partial pressure of oxygen. In conjunction with the focussed ion beam (FIB), we are investigating *in-situ* lateral pattern generation by selectively etching -- with

chlorine GBE -- those areas of the substrate that have been damaged by the FIB. We'll use chlorine GBE over chlorine RBE in the last two processes because the radical etch tends to leave behind a rougher surface, which creates problems for MBE regrowth.

We are studying IBAE and RBIBE with chlorine as the reactive gas in a *quasi in-situ* process. By this we mean a process in which the initial epi layers are partially processed using standard cleanroom techniques, but the critical regrowth surface is exposed under UHV conditions by etching in the processing chamber. Our process consists of forming a SiN_x layer on the epi material using standard lithographic techniques. The SiN_x is used as a sacrificial layer to transfer its pattern into the epi material. In our first try at this process, we etched (by RBIBE) 1.0 micron of a GaAs substrate in the time it took to etch away a 0.1 micron patterned SiN_x layer, giving a 10:1 GaAs: SiN_x etch rate selectivity ratio.

In Figure IV. 3. , some initial etch rate measurements for IBE and IBAE of GaAs are given for several argon ion beam conditions. A relatively high IBAE:IBE etch rate ratio of 31 was obtained for the lowest ion beam current (I_b) condition, indicating a largely chemical component in the IBAE case.

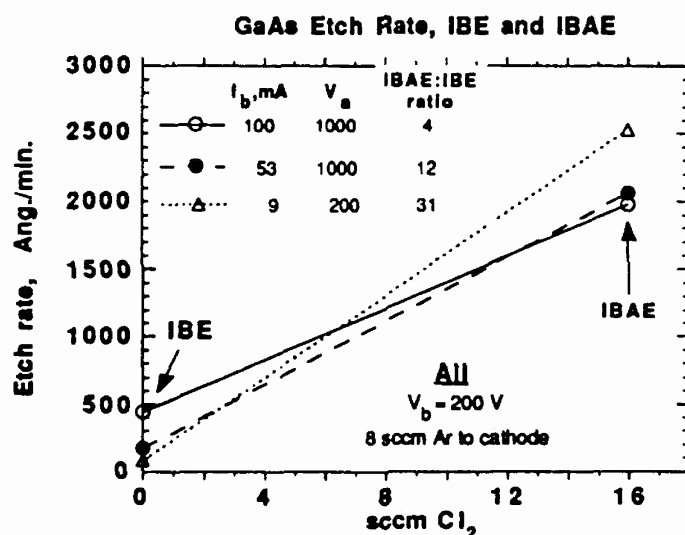


Figure IV. 3. GaAs etch rate data for three argon ion beam etch (IBE) conditions, and for ion beam assisted etch (IBAE) with 16 sccm Cl_2 . A relatively large IBE:IBAE etch rate ratio was obtained for the lowest ion beam current (I_b) case.

2. Substrate manipulator/stage

The substrate is transferred into the chamber and onto a molybdenum platten using a magnetically-coupled transfer tool similar to those used in our MBE machines. The platten is attached to a stage which can rotate the substrate in its own plane up to 10 RPM, for improved etch rate uniformity. The stage can be translated in the x-, y-, and z-directions via a bellows-sealed feedthrough and three micrometer controls, and it can be swung around to point the substrate at either the entry/exit port, the radical beam, or the ion beam. Substrate temperature is feedback-controlled with a pair of quartz halogen lamps and a thermocouple, with a maximum controllable temperature of 1000°C. The stage can be cooled with an alcohol/water solution. Special connector pins in the stage contact the Faraday cup to an ion current meter (the cup is negatively biased to repel neutralizer electrons, thus collecting only ion current). All feedthroughs are mounted on a custom-designed two-stage differentially-pumped rotatable seal made by Thermionics, Inc.

3. Analytical tools

The processing chamber has three tools used for in-situ process monitoring. 1) A Varian reflection high energy electron diffraction system, identical to those in the two MBE machines, is operational and we have obtained surface diffraction patterns; this system will be useful in studying the substrate surface quality following our H₂ and O₂ RBE preclean processes. 2) A state-of-the-art Spectramass, Inc. quadropole mass spectrometer has been used primarily as a residual gas analyzer and as a helium leak detector -- total pressure, in both cases, less than 10⁻⁵ torr; in the future we want to analyze etch products during the etch (10⁻⁵ to 10⁻³ torr) by installing a differentially-pumped chamber between the etch chamber and the mass analyzer. 3) We can measure etch rates of multi-layer epi material *in-situ* by detecting the light of a HeNe laser reflected off the etching surface and plotting the light signal, versus time, with a chart recorder.. The reflected intensity changes as a function of the refractive index of the epilayers, and a computer model written here is used to predict the shape of the chart recorder to use as a guide during the actual etch.

4. *Gas delivery and vacuum systems*

Before entering the chamber, all gases pass through a manifold box that is vented in case of a chlorine leak. Flow rates of the reactive gases and of the ion source/cathode argon are controlled with MKS mass flow controllers located inside the box; the neutralizer argon partial pressure is controlled with a low-flow, double-stemmed needle valve. All gas lines can be purged with ultra-high purity nitrogen and evacuated with a venturi pump. Two gas lines (chlorine and a spare) were designed for corrosive handling and have all-welded connections and corrosion-resistant Hastelloy C-22 tubing. The other gas lines' fittings are VCR-type, including all connections in the Ion Tech cathode and neutralizer. A safety interlock controller prevents undesirable gas mixtures (e.g., H_2 and O_2), and stops or prevents process gas flows if the tunnel gate valve is open, if the cryo temperature is not below a set value, or in the event of a chlorine leak (three chlorine sensors are located at the chlorine cylinder, in the manifold box, and outside the processing chamber); also, this controller will automatically close the chamber/cryopump gate valve and regenerate the cryopump if a compressor power failure lasts beyond a selected time (presently 10 minutes).

The cryopump is a Varian 8-inch model which we rough-down with venturi and vacsorb pumps. The chamber is similarly roughed-down to approximately 50 millitorr before opening the chamber/cryo gate valve. Chamber baking after venting to atmosphere is accomplished with heating pads wrapped around all the large flanges, and with a single quartz halogen lamp (controlled with a Variac) mounted under the stage in the middle of the chamber; standard chamber bake temperature is $150^\circ C$. We have three different pressure meters at our disposal: a convectron gauge, a hot cathode ion gauge, and a capacitance manometer. Our best ultimate base pressure to date (following a weekend bake) is 3.0×10^{-9} torr.

5. *Electron gun purchase*

We are in the process of purchasing an electron gun from FEI, Inc., which will be installed on the top flange of the processing chamber. The gun will be used in conjunction with chlorine

GBE to form patterns in substrates by selectively etching that part of the substrate exposed to electron current. The long working distance (up to 8 cm) of the FEI source allows us room to rotate our stage from the entry/exit position to the the ion beam without the need to raise the electron gun out of the way; in addition, the long working distance enables us to use a very small electron aperture to reduce the amount of chlorine that can get into the electron column, while still maintaining a relatively large field of view. An extra ion pump (two total) at the electron source will also help to reduce the chlorine pressure in the column. To improve the lateral etch resolution of the gun by reducing vibrations, we have installed both a pneumatically-damped bellows between the chamber and the cryopump and a mechanically-damped bellows between the chamber and the UHV tunnel (see Figure IV. 2). The entire chamber is bolted to a floating table. Another purpose of the electron gun will be to operate it in standard SEM imaging mode, allowing us to monitor our pattern generation processes *in-situ*.

C. Summary

The *in-situ* processing chamber has been designed, installed and demonstrated over the past year. It is part of a multichamber *in-situ* processing system that is capable of fabricating nanostructures in MBE epi material completely under UHV conditions. Our accomplishments to-date with the processing chamber include making initial IBE, IBAE and RBIBE etch rate measurements in the processing chamber, demonstrating a *quasi in-situ* process employing pattern transfer of a sacrificial SiN_x layer, and initiating experiments that will study *in-situ* pattern generation in conjunction with the FIB machine.

V. QUANTUM-WELL WIRE LASER

A. Introduction

Quantum-well wires, especially closely-packed arrays of quantum-well wires, should find important applications in optoelectronics. The additional quantum-mechanical confinement of a quantum wire beyond that of existing quantum wells -- thin sheets of material instead of thin wires -- increases the density of electronic states at a particular energy. Desirable devices arise from this increase, because the energy of an electrical current may be more efficiently converted into light and *vice versa*. Double heterostructure (DH) lasers, devices at the heart of optoelectronic systems, should benefit from the improvement of using quantum-well wire arrays, which promise lower operating currents and better temperature stability [6-8]. We have been developing separate confinement (SCH) lasers which contain active regions of coupled quantum wire arrays formed within a serpentine superlattice (SSL).

The effort to date on the SSL laser project has been three fold: Firstly, appropriate conditions have been established for the growth by molecular beam epitaxy (MBE) of DHSC SSL laser structures suitable for fabrication into working devices. This has required that a conventional DHSC growth process be modified to accommodate a SSL active region and that the entire structure be designed to accommodate the optical and electrical properties of a SSL prepared on a (100) vicinal substrate. Secondly, a fabrication procedure has been developed and qualified in order to evaluate the SSL laser structure. In-plane and ridge-waveguide SSL devices have been fabricated for characterization. The design rules for the ridge-waveguide structure have been developed and tested by fabricating single quantum-well (SQW) SCH devices that have GaAs and $\text{In}_{0.2}\text{Ga}_{0.8}\text{As}$ quantum-wells. Lastly, working devices have been characterized near room temperature, at 77 K and at 1.4 K. Light output *versus* operating current (L-I) curves have been taken, and spectra of the emitted light have been obtained which unambiguously demonstrate single-mode lasing. On going efforts are concentrated on establishing the effects of the SSL coupled quantum-wire array active region on the laser characteristics.

B. Layer design and growth

A conventional SCH laser structure has been selected for characterizing the electrical and optical properties of SSL quantum-well wires used for a gain medium. Figure V. 1 shows SSL layers incorporated into a broad-area laser structure. The layers are designed in such a way to have an optimized optical confinement factor for the fundamental transverse mode. They occur in the following order, from the substrate upwards: a GaAs/AlAs buffer superlattice, $1\mu\text{m}$ $\text{Al}_{0.8}\text{Ga}_{0.2}\text{As}$ n-cladding (Si-doped to $1 \times 10^{18} \text{ cm}^{-3}$), 470\AA $\text{Al}_{0.5}\text{Ga}_{0.5}\text{As}$ lower waveguide layer, 340\AA SSL active layer, 470\AA $\text{Al}_{0.5}\text{Ga}_{0.5}\text{As}$ upper waveguide layer, $1\mu\text{m}$ $\text{Al}_{0.8}\text{Ga}_{0.2}\text{As}$ p-cladding (Be-doped to $5 \times 10^{17} \text{ cm}^{-3}$), and then 1500\AA p⁺-GaAs capping layer.

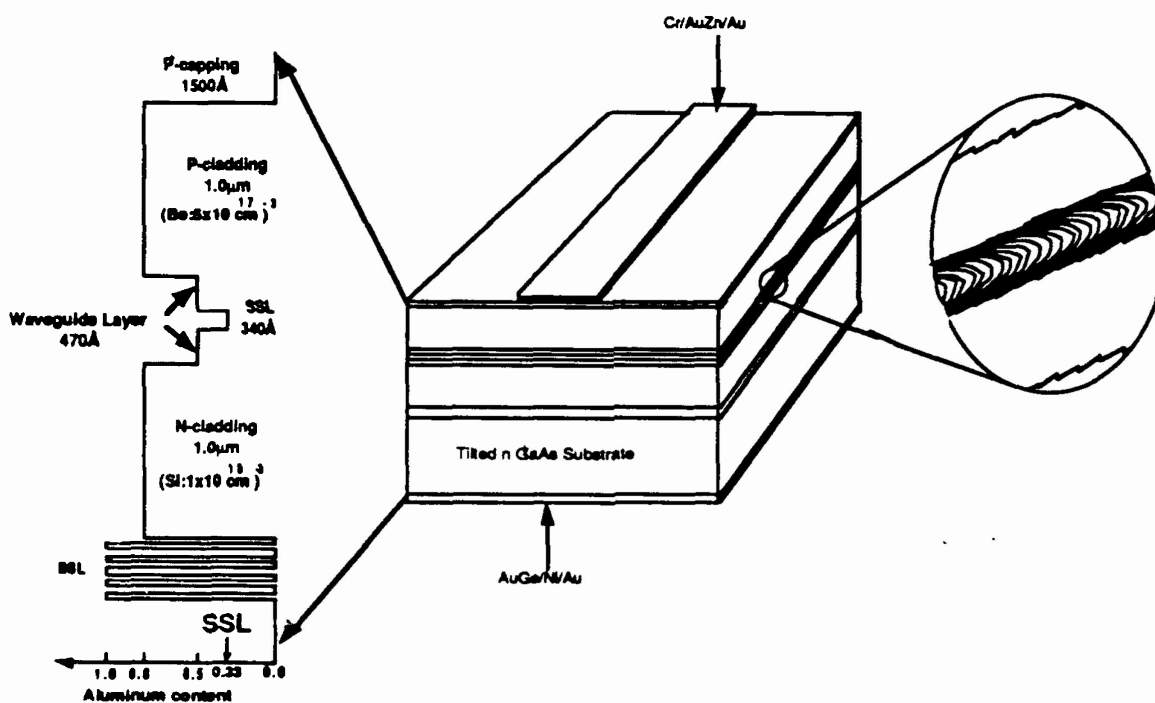


Figure V. 1. Layer Structure for the Serpentine Superlattice quantum-well wire lasers.

Including a SSL layer into a DH test structure has required adapting standard laser growth conditions to allow for the lower substrate temperatures and lower As pressures required for growing an SSL. The best conventional DH laser structures are grown at substrate temperatures

near 680°C and relatively high As beam pressures, which conflict with the 580-610°C substrate temperatures and As pressures, lower by a factor of three, needed to grow a SSL. Additionally, the best SSLs prepared to date are not ideally laterally separated into vertical wells and barriers; the AlAs of the barriers is partially distributed into the GaAs quantum wires. Because of this, and in order to maximize the confinement of the quantum wires, we have increased total AlAs content of the SSL up to a maximum which is limited by the direct-to-indirect bandgap transition in the (Ga,Al)As system. This AlAs content increase in the SSL has required corresponding increases in the AlAs content of the waveguide and cladding layers in order to achieve proper optical confinement. Several growths have been made to search for the optimal growth conditions for the laser structure. We have found conditions that satisfy the As pressure and substrate temperature requirements of the SSL and which allow the growth of a satisfactory DH SSL test structure prepared at lower substrate temperature and As pressure. The lower cladding layer has been modified to include a "dumping" superlattice just before the waveguide layer, which is a modification that has been previously demonstrated to give high quality, low temperature grown DH lasers. Further investigations will see SSL lasers which have less total AlAs in the SSL layer - - and thus lower overall AlAs content -- but the same degree of quantum confinement. Suitable model test structures are also currently being developed that, for example, replace the SSL active layer with an alloy layer of the same average AlAs content in order to decisively demonstrate the effects of the quantum wire array. The growth of such model samples have been attempted, though with unsatisfactory luminescence results. Preliminary investigations have also begun into fabricating quantum-well wire arrays on GaAs substrates that are misoriented from the (110) surface, instead of the misoriented (100) substrates of the lasers to date.

C. Device fabrication

Conventional broad-area and ridge-waveguide lasers were fabricated from the SSL laser epitaxial layers. Figure V. 1 shows the broad-area laser structure and Figure V. 2a illustrates the fabrication procedures for the ridge-waveguide lasers. The ridge is made by Cl₂ RIE with in situ

laser monitoring and polyimide is used as the dielectric isolation film. Cr/AuZn/Au and AuGe/Ni/Au alloy systems are chosen for the p- and n-contact metals, respectively.

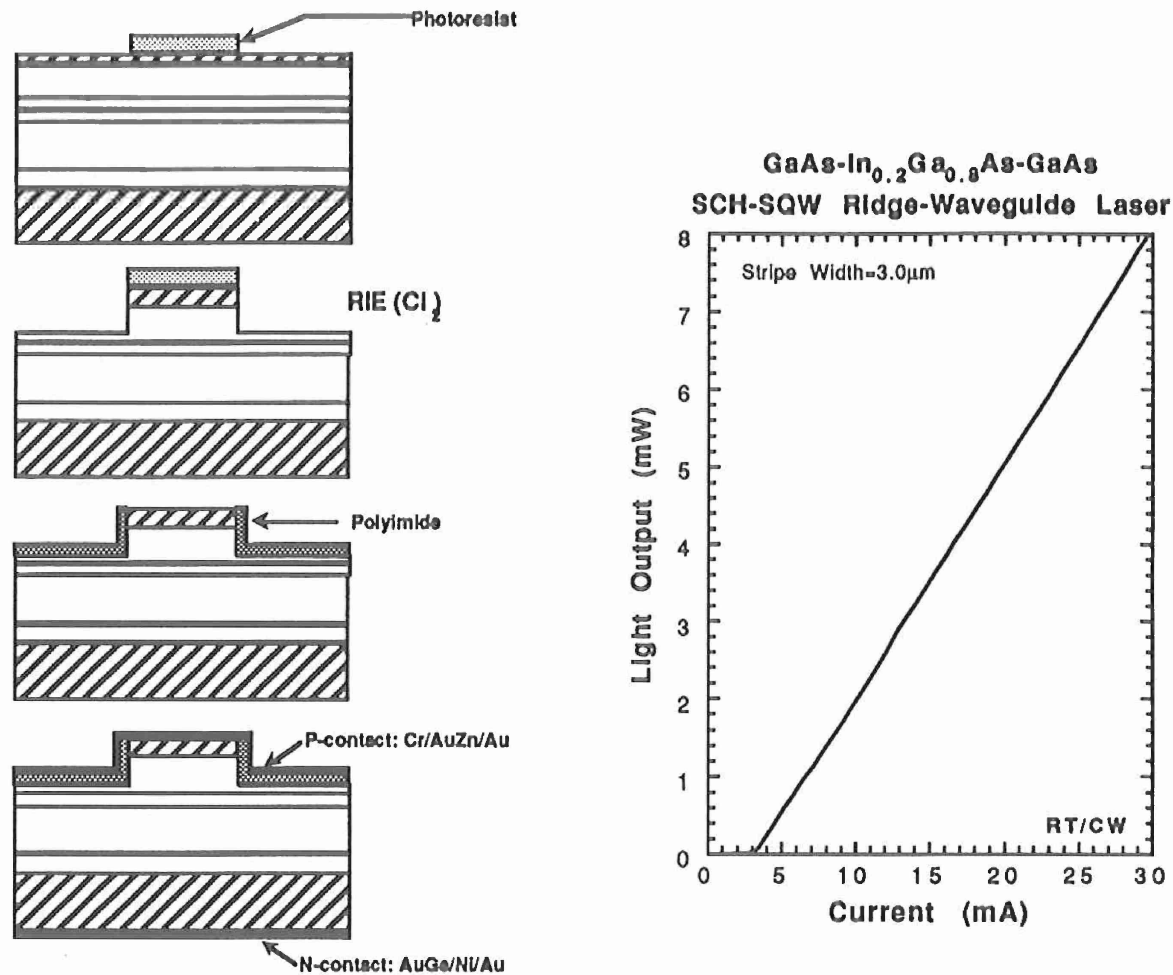


Figure V. 2(a) Ridge-waveguide laser processing (b) Demonstration of fabrication process using a strained-layer 3.0μm wide In_{0.2}Ga_{0.8}As ridge laser 210 μm in length.

To see wire effects, directions of the SSL laser cavities are arranged in either parallel or perpendicular to the wire directions. From anisotropy of gain spectra and threshold, it would be possible to identify the quality of the wires. Besides this, the alloy model sample can also tell us the difference with and without a SSL active layer.

Because the SSL laser samples are precious, a special effort has been made to optimize the ridge-waveguide laser fabrication process by working on GaAs and In_{0.2}Ga_{0.8}As single quantum-

laser monitoring and polyimide is used as the dielectric isolation film. Cr/AuZn/Au and AuGe/Ni/Au alloy systems are chosen for the p- and n-contact metals, respectively.

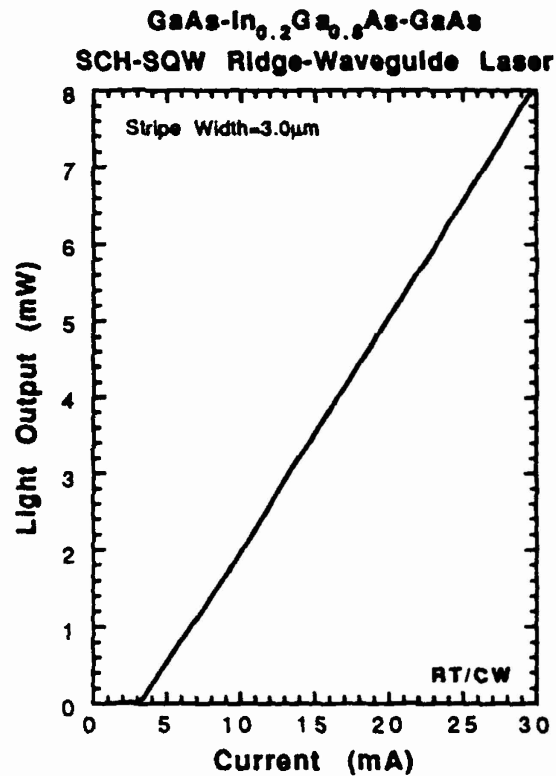
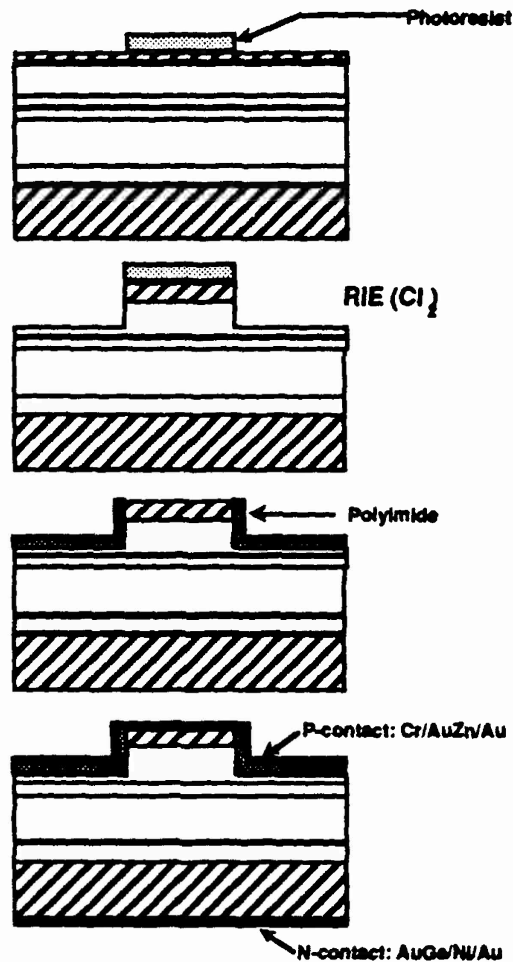


Figure V. 2(a) Ridge-waveguide laser processing (b) Demonstration of fabrication process using a strained-layer $3.0\mu\text{m}$ wide $\text{In}_{0.2}\text{Ga}_{0.8}\text{As}$ ridge laser $210\mu\text{m}$ in length.

To see wire effects, directions of the SSL laser cavities are arranged in either parallel or perpendicular to the wire directions. From anisotropy of gain spectra and threshold, it would be possible to identify the quality of the wires. Besides this, the alloy model sample can also tell us the difference with and without a SSL active layer.

Because the SSL laser samples are precious, a special effort has been made to optimize the ridge-waveguide laser fabrication process by working on GaAs and $\text{In}_{0.2}\text{Ga}_{0.8}\text{As}$ single quantum-

well SCH structures. It is found that the choice among SiO_2 , Si_xN_y and polyimide as the dielectric film is not critical, but the etching depth in the RIE process is directly related to the device performance. The height of the ridge determines the optical confinement as well as the lateral diffusion of the injected carriers. Furthermore, if the active layer is etched and exposed along the ridge sidewalls, surface recombination will also play an important role in determining the device threshold. A more quantitative study is in process, but it is clear qualitatively that the position of the etching stop in the $\text{AlGaAs/GaAs/AlGaAs}$ QW or QWW structures should be above the active layer (at least within a certain region adjacent to the ridge.) The in situ laser monitored dry etching technique has been used in our device processing and it makes precise etching-depth control become possible.

In the process of reducing the series resistance in the I-V characteristics of narrow-stripe devices, a dry-then-wet etch technique was developed. First, we use Cl_2 RIE to form a wider ridge and then use buffered HF to undercut the $\text{Al}_{0.8}\text{Ga}_{0.2}\text{As}$ cladding layer. In this configuration, a wider contact area is retained while the effective stripe width is still very narrow, for example, $1.4\text{ }\mu\text{m}$ or even smaller. The optimal effective ridge width is found at the $2.5\sim 3.0\text{ }\mu\text{m}$ range for $\text{In}_{0.2}\text{Ga}_{0.8}\text{As}$ SQW-SCH lasers. From a $3.0\text{ }\mu\text{m}$ effective stripe width $\text{In}_{0.2}\text{Ga}_{0.8}\text{As}$ SQW-SCH *mushroom ridge-waveguide laser*, 3.2mA low threshold has been obtained (Figure V. 2b.) The advantage of this new scheme over the conventional wet-etch-only method is that the ridge sidewall can be smoother, and steeper. For this device structure, polyimide is the only usable dielectric. In the next step, we are going to incorporate this structure onto the SSL laser samples.

D. Device characterization

SSL lasers are being tested at various temperatures. Initial thresholds have been high due to poor carrier confinement in the first design. Thus, lasing behavior is observed only at temperatures slightly below room temperature, and the output light intensity is a sensitive function of temperature. At 280°K , the average threshold current is 120mA from $3\text{ }\mu\text{m}$ devices of either orientation. At liquid nitrogen temperature, an orientation dependence is observed. Figure V. 3

shows the light-current characteristics of a $3.8\mu\text{m}$ -stripe-width device in which the propagation direction is perpendicular to the wires. A 2mA threshold and an external quantum efficiency of 38.7% at 77°K is observed. The thresholds for propagation along the wires are higher, but a large variation in threshold is observed, possibly due to a non-uniformity of the wires across the wafer. However, samples with an optimum combination of layer compositions have not yet been properly grown, so results could improve significantly.

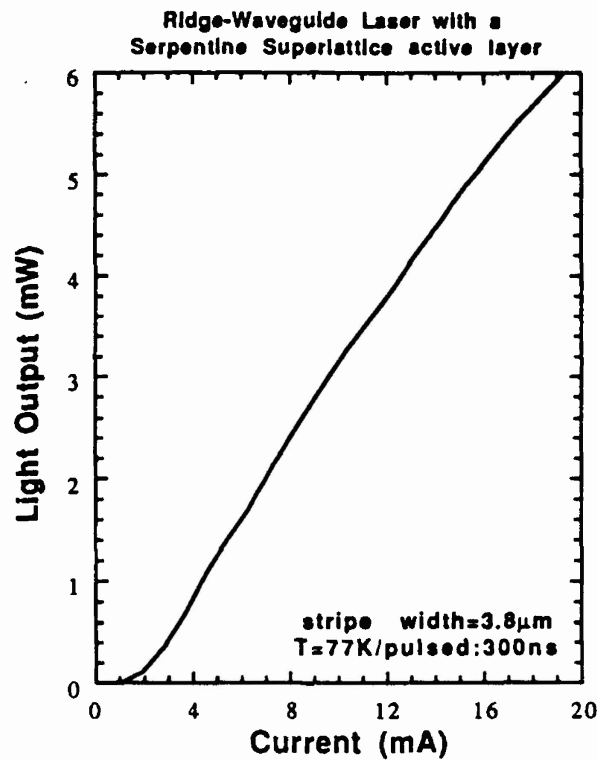


Figure V.3. Light-current characteristic of a $3.8\mu\text{m}$ wide SSL ridge laser measured at 77°K.

VI. THEORETICAL CHARACTERISTICS OF QUANTUM-WIRE STRUCTURES

A. Introduction

In this section the theoretical density of states functions and the resulting laser gain characteristics for TSLs and SSLs are summarized [9,10]. For reference, Figures VI. 1(a) and (b) show cross sectional profiles of TSLs and a SSLs as introduced above. As already discussed, a TSL or SSL is directly grown on an off-axis or vicinal GaAs substrate by alternating deposition of two materials of different compositions by either MBE or MOCVD. The end result is an array of quantum well wires (QWW) with a period T , which is determined by the tilt angle, α of the substrate. These structures have several significant advantages in comparison with the arrays of QWW fabricated with fine line lithography techniques. The lateral dimensions are in the low nanometer range which is suitable for obtaining sufficient quantum size effect, they are obtained processing free; hence, they are free from processing damage. As already discussed the SSL should be more immune to substrate surface and growth rate variations[4]. For the desired sharp spectral gain characteristics, it is important that the quantum-wire subband spacing be larger than the thermal energy and that any broadening of the energy levels due to unavoidable imperfections is also much less than this subband separation.

In the analysis, the finite element method (FEM) was used to solve the Schrödinger equation [11]. Particularly for the case of superlattices, the potential profile is periodic. So one can simplify the wavefunction by using the Bloch theorem, which states that the wavefunction in one cell is exactly the same as that in the adjacent cell except for a phase term e^{-jkT} , where k is the Bloch wavenumber and T is the width of a period. The application of periodic boundary conditions enables one to analyze an infinite array of QWR and create the E-k diagram from which the DOS function of the superlattice can be directly obtained.

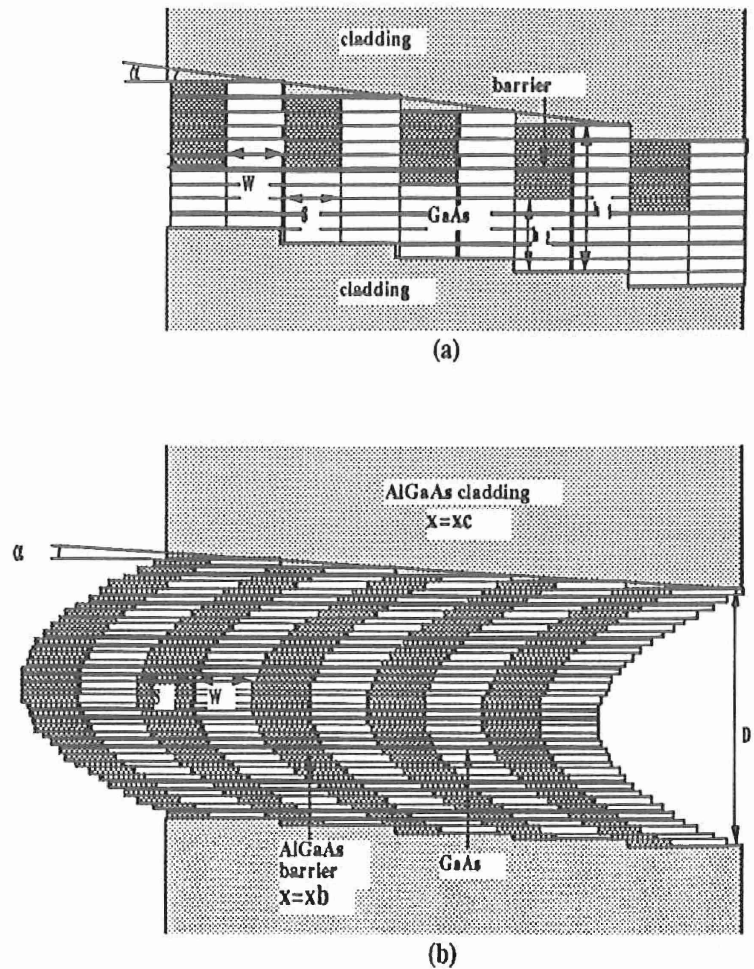


Figure VI. 1. (a) Schematic cross sectional profile of a TSL; (b) Schematic cross sectional profile of an SSL.

B. TSL Results

In Figure VI. 2(a), the conduction band DOS curves are shown for the TSL structures as a function of the coupling layer thickness, h_2 , which varies from 0 to h_1 . The thickness of TSL, h_1 , is 100 Å, the widths of the wire and barrier, W and S , are both 40.5 Å, and the Al compositions in the cladding and barrier, x_c and x_b , are both 0.25. When h_2 is 0, then the TSL is an array of rectangular QWR's and the DOS show a profile with sharp peaks. As h_2 increases, the DOS becomes broadened due to the increased coupling between wires, and when $h_2=h_1$, the TSL becomes identical to quantum well structure and shows a step like DOS curve. In this structure, even for the rectangular wire case, i.e., when $h_2=0$, the DOS is far from the ideal QWR DOS curve where we expect a sharply localized shape. The broad DOS curve is due to a finite wire-to-

wire coupling since the barrier height and width are relatively small. This coupling broadens the individual eigenstates of single wires into minibands. Furthermore, the subband spacing is only 30 meV which is at the order of the thermal energy ($k_B T$) at room temperature. In Figure VI. 2-b, the DOS curves for another TSL structure are shown where x_b is increased to 0.5 and x_c to 0.4. For this structure, when h_2 is 0, the DOS becomes sharply peaked and well localized due to the negligible coupling between the wires. And the subband spacing is also increased to 75 meV. Even when h_2 is increased up to 20 Å, the subband spacing is still larger than 50 meV and the DOS curves are still well localized. So the structure with higher x_b and x_c is more desirable for the realization of true quantum wire laser since it gives a sharper DOS curve and larger subband spacing. If x_b and x_c are increased further, however, the optical confinement becomes poor and the carrier loss due to the L- and X-valley becomes dominant. So the optimum Al composition around quantum wires should be ~ 0.5 .

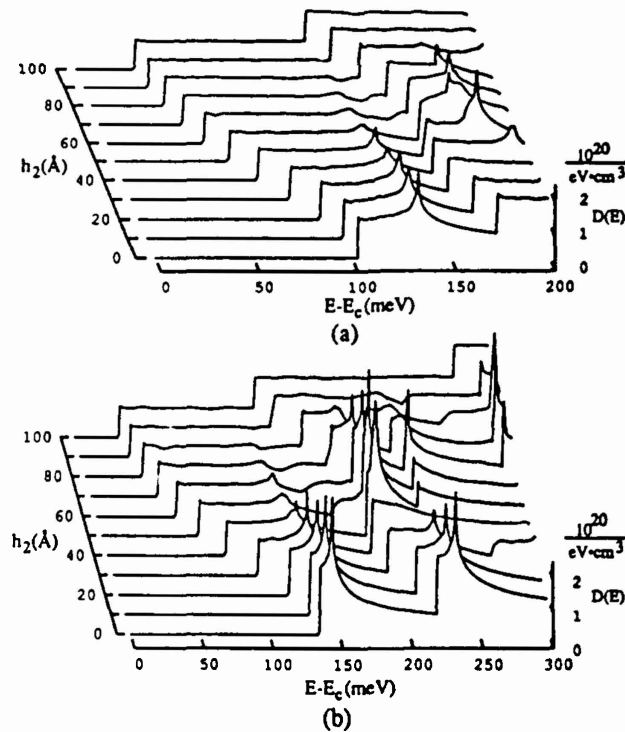


Figure VI. 2. Conduction band density of states of a TSL versus electron energy above the conduction band minimum for different values of h_2 . (a) $h_1=100\text{Å}$, $W=S=40.5\text{Å}$, $x_b=x_c=0.25$, $h_2=0-h_1$. (b) $h_1=100\text{Å}$, $W=S=40.5\text{Å}$, $x_b=0.5$, $x_c=0.4$, $h_2=0-h_1$.

In Figure VI. 3, the gain curves are plotted for the TSL with $W=S=40.5 \text{ \AA}$, $h_1=100 \text{ \AA}$, $h_2=0 \text{ \AA}$, $x_b=0.5$, $x_c=0.4$ for three different electric field polarizations. In this calculation, a 4 band $k \cdot p$ analysis is used to calculate the valence band structure. The modal gain is obtained at 300K with $n_s=4 \times 10^{18}/\text{cm}^3$, $\tau_{in}=0.1 \text{ ps}$, and $\Gamma=0.023$, where n_s is the injected carrier density, τ_{in} is the intraband relaxation time, and Γ is the optical confinement factor. The gain curve of this TSL is sharply localized and high compared to quantum well structure for the same n_s . The gain curves also show strong polarization dependence. When the electrical field polarization is parallel to the axis of the wires, i.e., along x direction, the gain is significantly enhanced, whereas it becomes suppressed when electrical field is polarized in y direction. These two polarizations correspond to a TE polarized optical mode. If the electric field polarization is in z direction, which corresponds to a TM polarized optical mode, one still observes a high gain. But the peak of this gain is about 67% of the maximum gain for x polarization. So, the largest anisotropy can be observed between x and y polarization, i.e., the two mutually orthogonal TE polarizations. This suggests that easier single polarization lasing could be achieved when light propagates perpendicular to the TSL plane, i.e., in z direction, as in the vertical cavity surface emitting laser.

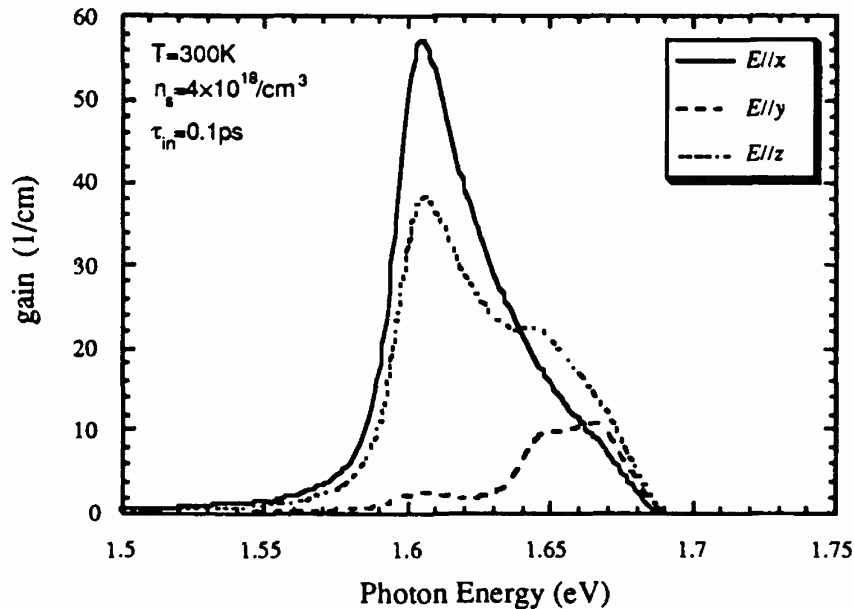


Figure VI. 3. Modal gain of a TSL for different electric field polarizations. $h_1=100 \text{ \AA}$, $h_2=0 \text{ \AA}$, $W=S=40.5 \text{ \AA}$, $x_b=0.5$, $x_c=0.4$.

This TSL structure can be further optimized by controlling the substrate tilt angle, α . By reducing the substrate tilt angle, the barrier and well widths can be increased. Therefore, the wire-to-wire coupling reduces and the DOS curves become sharper and better localized. However, one cannot reduce α arbitrarily because as α decreases, the growth becomes more difficult and the wire density in TSL decreases. A tilt angle of 1.5° seems to be a good compromise between wire to wire coupling and fabrication difficulties.

In practice, however, TSL's have been far from being ideal. The interfaces between wires and barriers are subject to fluctuate due to the growth rate fluctuation. Furthermore, the growth interface may tilt if the growth rate does not have the correct nominal value. As a result, experiments have not gained the same degree of polarization anisotropy predicted in Figure VI. 3. However, 30 % anisotropy has been observed between x and y polarization [12,13]. The effects of such imperfections on the miniband characteristics of TSL are also analyzed. In the analysis, the wire widths are assumed to fluctuate randomly from their nominal position with a standard deviation of 6 \AA , which corresponds to approximately one lattice constant. The interfaces are also assumed to tilt randomly up to 20° , which corresponds to about a 1 % departure from the correct growth rate. The variation of the upper and lower ends of the lowest miniband as a function of h_2 are shown in Figure VI. 4 for 1.5° off TSL. The hatched area indicated as the ideal miniband is due to wire to wire coupling in the ideal structure and becomes negligible as h_2 goes to zero. The dark area indicated as broadened miniband is due to imperfections in the structure and becomes quite small as h_2 approaches h_1 . The overall miniband width becomes minimum at a non-zero h_2 value, in this case, at $h_2=20 \text{ \AA}$. Therefore, the introduction of a thin coupling layer between the wires and hence a slight delocalization of the electron wavefunction helps to reduce the quantized energy level broadening [13].

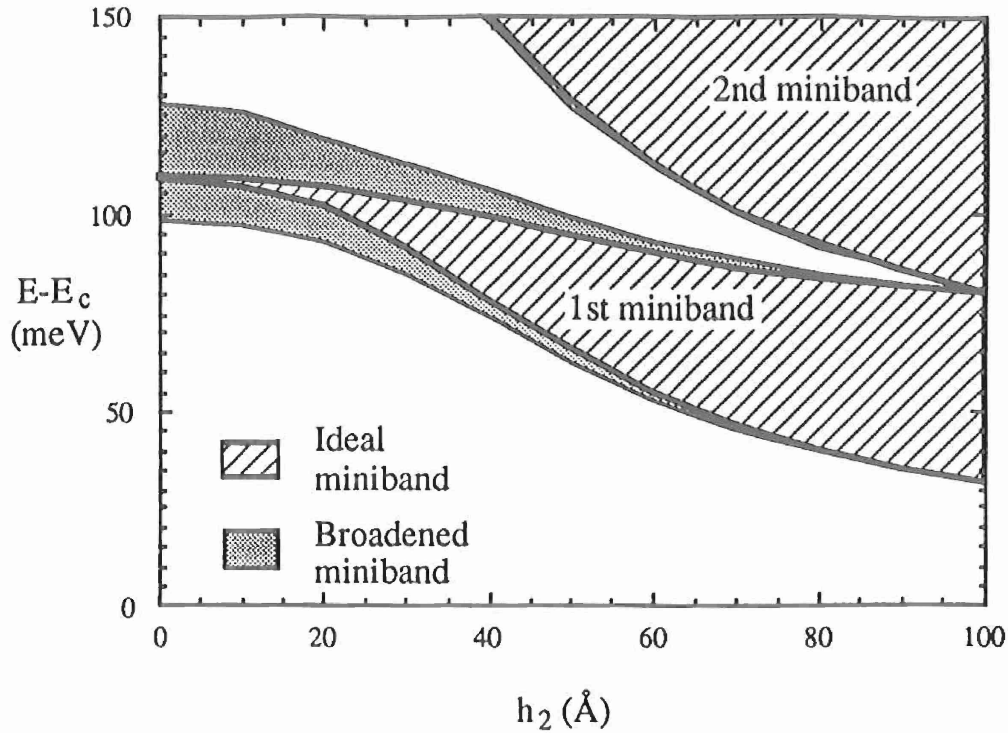


Figure VI. 4. Variation of the upper and lower edges of the first miniband of a TSL as a function of h_2 . Hatched and dark areas designate the miniband under ideal and non-ideal conditions, respectively. $h_1=100\text{\AA}$, $W=S=54\text{\AA}$, $x_b=0.5$, $x_c=0.4$, $h_2=0\sim h_1$.

C. SSL Results

For the SSL, the growth time per cycle is deliberately varied to vary the TSL tilt angle. The net curvature of growth interface, hence degree of confinement, depends on the substrate tilt angle, the maximum variation of the growth rate, and the total thickness of the SSL. These, plus the Al content in the barriers and the claddings, are the parameters that are available to engineer the structure. Figure VI. 5. shows the variation of the subband spacings and widths of a SSL on 2° vicinal GaAs substrate, i.e., when $W=S=40\text{\AA}$, as the tilt parameter p , which is directly proportional to the growth rate, is varied $\pm 20\%$. The wire material is GaAs and x_b and x_c are 1.0 and 0.4 respectively. When $\Delta p=0$ the SSL is nothing but a long and narrow rectangular structure and the subband spacing is very small. However, as Δp increases curvature of the growth interface increases, hence the confinement increases, increasing the subband spacing. The widths of the minibands for the higher subbands also become wider. This is due to excessive coupling

between the wires and as a result the energy levels are broadened into minibands. In this case even the use of the highest possible Al content in the barriers does not eliminate this problem completely. However, additional calculations indicate that the use of substrates with 1° misorientations indicate much wider miniband spacings and less wire-to-wire coupling.

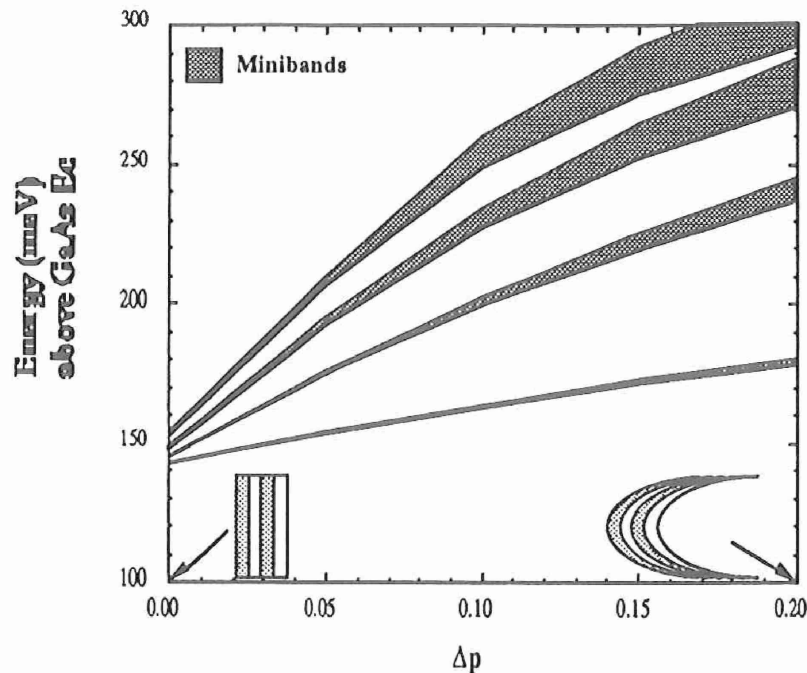


Figure VI. 5. Variation of the subband spacings and widths as a function of the growth rate variation for a SSL with $x_b=1.0$, $x_c=0.40$, $W=S=40\text{\AA}$, $D_0 = 920\text{\AA}$ as the growth rate varies $\pm 20\%$ during growth ($\Delta p=\pm 20\%$).

The corresponding density of states (DOS) in the conduction band is shown in Figure VI. 6. As Δp increases one obtains a strong localization and quantum wire like behavior. Another way to increase the subband spacing is to increase the well and barrier widths by increasing the tilt angle of the substrate. For a 1° off substrate well and barrier widths can each be increased to 80\AA , hence the wire to wire coupling, miniband formation and broadening of the DOS can be reduced significantly. Another alternative to reduce the subband spacing is to reduce the total thickness of the SSL, which results in higher curvature and higher confinement.

Figure VI. 7. gives the SSL gain characteristics for an example case. Here to be more realistic, the barrier material is assumed to have only 50% Al, but the curvature is increased by

using only a 460\AA SSL thickness to further separate the minibands. To account for finite state lifetime and some inhomogeneous broadening, a net ΔE of 5meV is assumed.

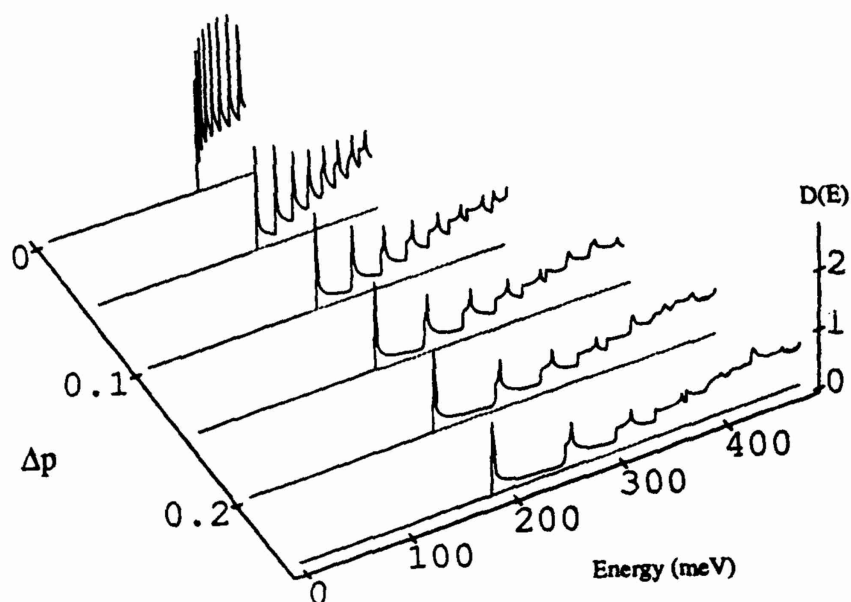


Figure VI. 6. Conduction band density of states ($10^9/\text{eV}\cdot\text{cm}$) of a SSL with $x_b=1.0$, $x_c=0.40$, $W=S=40\text{\AA}$, $D_0 = 920$, and $\Delta p=\pm 20\%$.

Gain curves of SSL

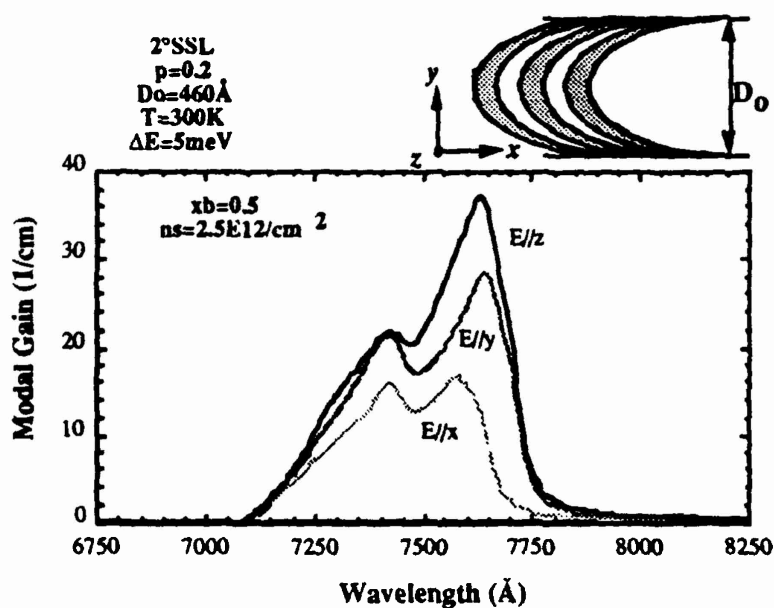


Figure VI. 7. Modal gain for SSL structure defined by indicated parameters.

VII. VERTICAL-CAVITY SURFACE-EMITTING LASERS

A. Introduction

The work on vertical-cavity surface-emitting lasers (VCSELs) during the past contract year has been divided over several funding sources. This ARO/SDIO program has supported some of the basic MBE technology for several different device structures as well as most of the device work on one specific structure. Thus, we shall here emphasize this one structure, but we shall also briefly review the progress on the VCSEL program as a whole.

One of the early myths about VCSELs, which can still be heard today, was that because the gain length was so short, it would be difficult to get much power out of these devices. For indirect reasons, such as difficulty in heat sinking and high series resistance, there is some truth to the conclusion, but not for the inherent reasons that have been argued by some highly respected workers in the field. They have argued that for such a short gain length, the mirror reflectivity must be very high to obtain lasing, and thus, only a very small fraction of the light in the cavity could be coupled out above threshold, leading to a very small quantum-efficiency. Unfortunately, many of the early experimental devices were designed to have very low quantum-efficiencies, adding to the credibility of this argument. But, if one actually carries the calculations through, it becomes clear that properly designed VCSELs indeed should have very similar threshold current densities and differential quantum efficiencies to conventional in-plane lasers. In the case of the differential efficiency, the basic reason for this similarity is that the net internal loss per round trip is reduced by about as much as the mirror transmission. Thus, the ratio of the output coupling to the total loss per round trip can still be large. In fact, the direct consequence of a small active volume is a small threshold current, not a small output power.

B. Calculations

For short in-plane lasers, Harder, et al [14] have correctly shown that if the cavity lifetime is kept constant as the cavity length is shortened, then the terms in the threshold gain equation remain the same, and as a result, both the threshold gain and the differential efficiency remain the

same. Keeping the cavity lifetime constant as the cavity length L is shortened, is accomplished by increasing the mean mirror reflectivity R in the mirror loss term α_m in the well known equation for threshold gain g_{th} :

$$\Gamma g_{th} = \alpha_i + \alpha_m = \alpha_i + (1/L)\ln(1/R) \quad (1)$$

Of course, in this case the lateral confinement factor Γ , and the average internal loss α_i , are assumed to not change with cavity length. If α_i and α_m as well as the internal efficiency η_i do not change, then there is also no change in the external differential efficiency η_{ex} as the cavity length is changed:

$$\eta_{ex} = \eta_i \alpha_m / (\alpha_i + \alpha_m). \quad (2)$$

For the VCSEL, however, we must go back one step in the derivation of Eq. (1) to explicitly include different lengths for the active gain region L_a and cavity L_c . Then we have,

$$\Gamma g_{th} L_a = \alpha_i L_c + \ln(1/R). \quad (3)$$

Dividing through by L_a , we get a properly modified Eq. (1):

$$\Gamma g_{th} = (L_c/L_a)\alpha_i + (1/L_a)\ln(1/R). \quad (4)$$

In a VCSEL, L_a is the vertical thickness of the active region, which may be just the thickness of one or two quantum-wells, and L_c is the effective cavity length of the DBR laser measured between the equivalent reflection planes of the multielement mirrors. (For AlAs/GaAs, the penetration depth to the equivalent mirror plane is about $0.5\mu\text{m}$.) For a VCSEL, the lateral confinement factor Γ is typically much larger than that of a quantum-well in-plane laser. (Relative to that for a single-

quantum-well in-plane design, Γ for a VCSEL may be 20 to 30 times larger!) Finally, for a VCSEL, the effective vertical gain can be twice as large as the in-plane traveling wave gain for a given current density due to the periodic gain effect mentioned earlier. (That is, if the gain segment is narrow and placed at the E-field standing wave peak, where the square of the optical E-field is twice its longitudinal spatial average, then the net gain imparted is twice the incremental traveling wave gain.)

It may now be instructive to compare the various terms in Eq.(4) for "typical" in-plane and VCSEL lasers. Using subscripts 'vc' for VCSEL and 'ip' for in-plane, it can be seen that if we assume $(L_c/L_a)_{vc} \sim 50$, $(L_c/L_a)_{ip} \sim 1$, $\Gamma_{vc}/\Gamma_{ip} \sim 25$, $g_{vc}/g_{ip} \sim 2$, $\alpha_{ivc}/\alpha_{iip} \sim 1$, the left-hand sides and the first terms on the right-hand sides of Eq. (4) for both cases can be identical, if we multiply the in-plane equation through by 50. Now, if we wish the mirror loss terms to also be equal, we require that

$$50[(1/L_a)\ln(1/R)]_{ip} = [(1/L_a)\ln(1/R)]_{vc}. \quad (5)$$

Further assuming that $L_{aip}/L_{avc} \sim 10^4$, (e.g., 200 μm and 200 \AA , respectively) and that $R_{ip} \sim 0.32$, we find that $R_{vc} \sim 0.994$. Thus, for this mirror reflectivity and the other assumptions, the threshold current density and the differential quantum-efficiency will be the same for the example in-plane and VCSEL cases. However, it should be clear that this does not come about from the simple scaling outlined by Harder, et al, since each of the terms in the VCSEL threshold gain equation are all 50 times larger here. This is due to the geometrical enhancements in the lateral confinement factor (x25) and gain (x2) in the VCSEL. If it weren't for these features, the nay sayers would have been right! Also, it should be realized that the essence of this comparison does not change if a very short in-plane laser is used, since the in-plane mirror reflectivity is scaled-up according to Harder's recipe, which is basically to keep the factor within the brackets in Eq. (5) fixed.

The weakest assumption in the above example is that the average internal losses are equal. Actually, the internal losses for VCSELs may have to be larger due to high doping to try to reduce the series resistance. Currently, these losses are much larger in experimental VCSELs due to large optical scattering and diffraction losses as well as free carrier absorption. On the other hand, yet to be revealed innovations may lead to VCSELs with internal losses not significantly larger than current in-plane lasers.

As will be discussed below, fairly detailed calculations have recently been carried out for the traveling wave gain obtainable with both strained and unstrained quantum wells [15]. These calculations include the effects of band mixing in the valence band and the resulting non-parabolicity. As many have predicted, the results show that strained quantum wells are desirable because of their higher obtainable gain, their lower transparency value and their higher differential gain.

Figure VII. 1 summarizes the radiative current required for both threshold and 1 mW out of strained-layer VCSELs, which have a 10 μm diameter and $\alpha_i = 30 \text{ cm}^{-1}$, vs. the mean mirror reflectivity. The corresponding current density is given by the right ordinate, and the differential efficiency ($\eta_i = 1$) is given by the top abscissa. With this level of internal loss and the assumed AlAs/GaAs DBR mirrors, the optimum number of 80Å $\text{In}_{0.2}\text{Ga}_{0.8}\text{As}$ quantum-wells for lowest current @ 1mW is approximately 2 or 3. Also, the optimum mean mirror reflectivity is ~ 0.994 , the agreement with our earlier handwaving arguments being somewhat fortuitous. Figure VII. 1 is the most up-to-date version of the result originally reported in [16] for thicker active regions. Basically, it says that it is possible to get 1 mW out of a relatively large, high-loss VCSEL with less than 2 mA of drive current. Of course, nonradiative recombination and potential current and carrier leakages are neglected. In our initial experiments [17, 18], we have found that about half of the current is being lost to leakage and/or nonradiative processes, leading to about twice the predicted thresholds and half the predicted differential efficiencies. The results of others are in this same ballpark. However, it seems likely that experiments will move closer to theory as time goes on. In fact, a factor of two from optimum is amazingly good for such an early stage of research.

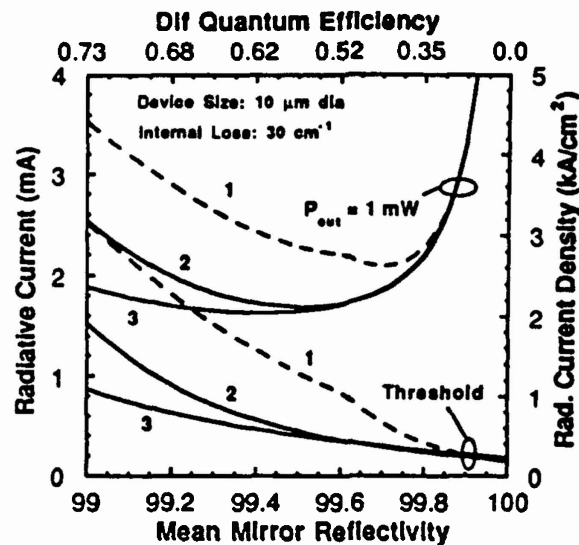


Figure VII. 1. Radiative current and current density vs R required for both threshold and 1 mW of power out for $\text{In}_{0.2}\text{Ga}_{0.8}\text{As}$ strained 80Å quantum-well SEL design curve labels 1-3 refer quantum efficiency is also shown for the assumed material loss of 30cm^{-1} and AlAs/GaAs DBR mirrors.

C. Transversely Pumped Periodic Gain Structure

The specific device structure that has been investigated under this program is illustrated in Figure VII. 2. As can be seen it is a further evolution of the transversely contacted periodic-gain structure originally invented by the UCSB group several years ago. However, we now show that by ion-implanting the p and n-type impurities on alternate sides of the nipi periodic gain structure, very uniform vertical waveguide structures can be formed. Once the implant is annealed, the mirror layers as well as the quantum-well active region intermixes. The I-V characteristics are rectifying, and the series resistance and voltage appear to be desirably small. Current efforts also include a one period version of the structure of Figure VII. 2. This turns out to be only a minor variation from another structure that we have been pursuing, shown in Figure VII. 3. As indicated, in this case it is also possible to use a conducting substrate. Current can be channeled through the active region by a buried implant or a constricted mesa etch. Again, we have measured good I-V characteristics for this structure, and for a version without the constricted mesa etch, we

have made electrically pumped lasers. These have operated with threshold currents $\sim 10\text{mA}$ with $\sim 2\%$ differential efficiency, owing to the fact that more than eighty percent of the current was not flowing through the active region between the mirror stacks, but rather conducting directly from the p-type contacts to the substrate. The constricted mesa versions are currently under fabrication.

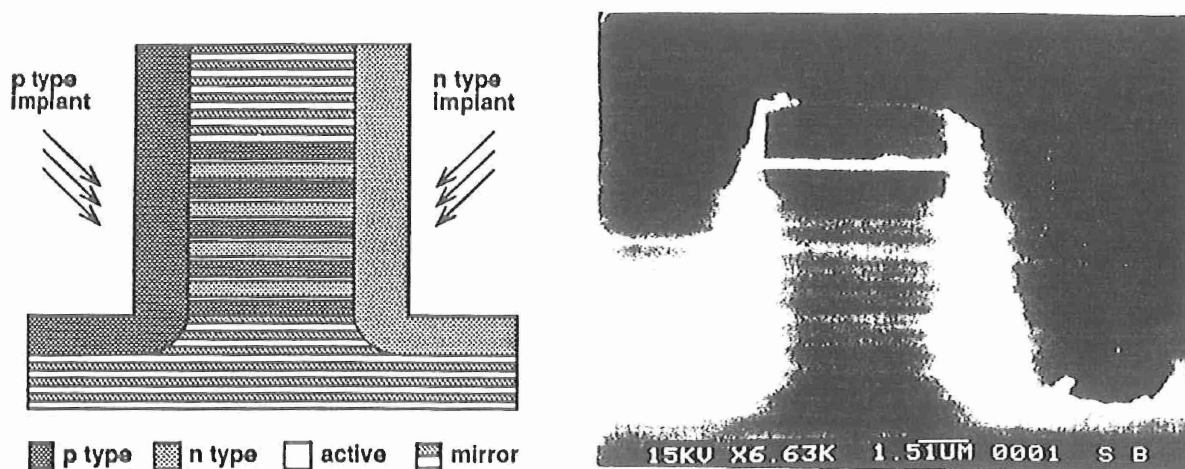


Figure VII. 2. Top VCSEL structure with implanted dopants on ridge sides to provide contact to lateral pumping layers. (a) Schematic of device showing as grown and implanted dopants. (b) SEM cross-section of implanted device showing disordering of mirrors and active regions.

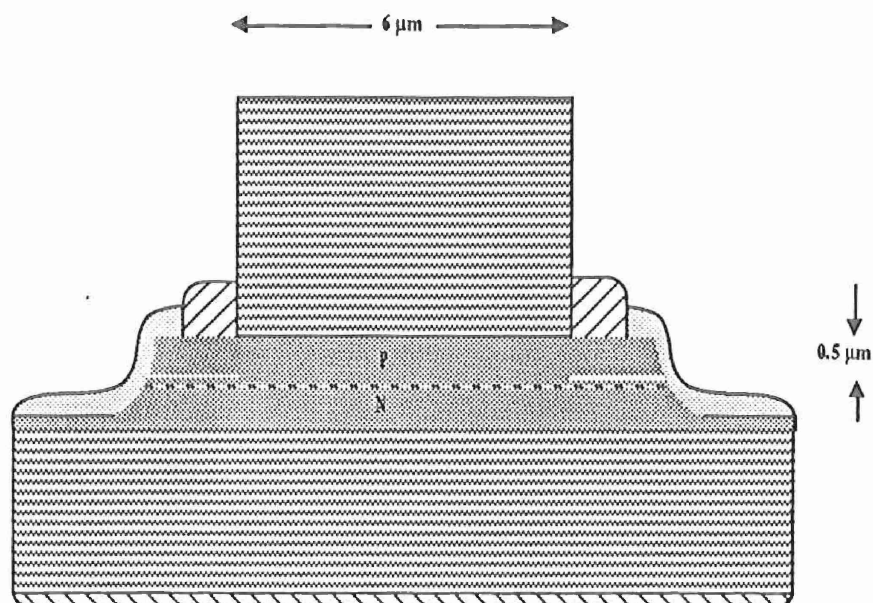


Figure VII. 3. Single-active-element, laterally-pumped structure with selective under etching to confine current.

D. Top-to-Bottom Pumped VCSELs

Figure VII. 4 gives the structure of a VCSEL which was designed with mirror reflectivities considerably higher than optimum for maximum power out. The objective was to obtain very low threshold currents. The theoretical mirror reflectivity was about 0.9996. Experimental values of threshold current and differential efficiency are consistent with a value larger than 0.999, dependent upon assumed internal losses and quantum efficiencies. However, if the above summarized gain calculations are assumed to be correct, then a value ~ 0.9996 is suggested. Figure VII. 5 gives the measured pulsed and cw L-I characteristics of one such device, and Figure VII. 6 gives cw threshold current values of all devices across one chip. As can be seen, cw threshold currents as low as 0.7 mA were obtained. On broader area devices threshold current densities of 600 A/cm^2 were measured. Of course, due to the high mirror reflectivity, the power out and the differential efficiency were limited. More recent broad area devices designed with more optimal mirror reflectivities ($R = 0.995$) and two 80\AA InGaAs quantum wells gave $\sim 25\%$ differential efficiencies with still less than 1 kA/cm^2 of threshold current density. Substrate absorption losses may also account for some of the reduction in differential efficiency in all of these bottom surface-emitting strained-layer devices.

In all of the above experiments series resistance and excess voltage drop remains a problem. For the $7\mu\text{m}$ square 0.7 mA device the applied voltage at threshold was 3.5V. The differential series resistance above threshold was $\sim 1.1 \text{ k}\Omega$ due to the fairly large turn-on voltage. Part of the problem in this case was due to the excessive mirror length. With the shorter 14 period mirrors used in the more optimal mirror case above, this turn-on voltage was considerably lower. However, this turn-on voltage drop and series resistance remain areas of primary concern. Other important characteristics of VCSELs include their spectral linewidth and far-field diffraction angle. Measurements have been made on devices from the initial batch with the high mirror reflectivities. Briefly, far-field angles in both 7 and $12 \mu\text{m}$ square devices were near the diffraction limits, corresponding to a FWHM of $\sim 5^\circ$ in the $12 \mu\text{m}$ case. In order to determine the laser

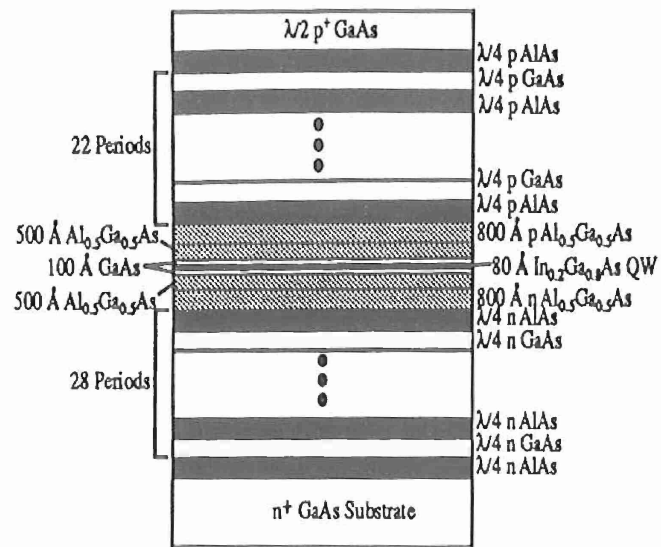


Figure VII. 4. VCSEL material structure.

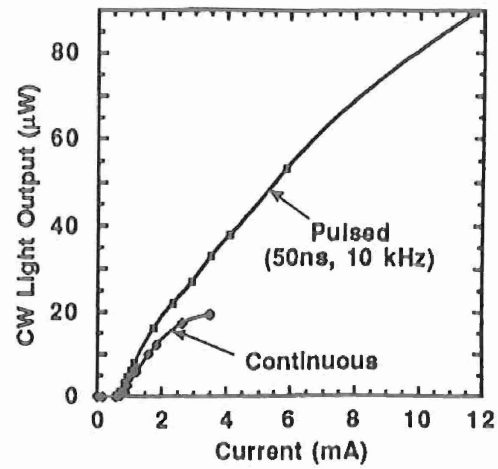


Figure VII. 5. Light vs current for 7 μm square SEL.

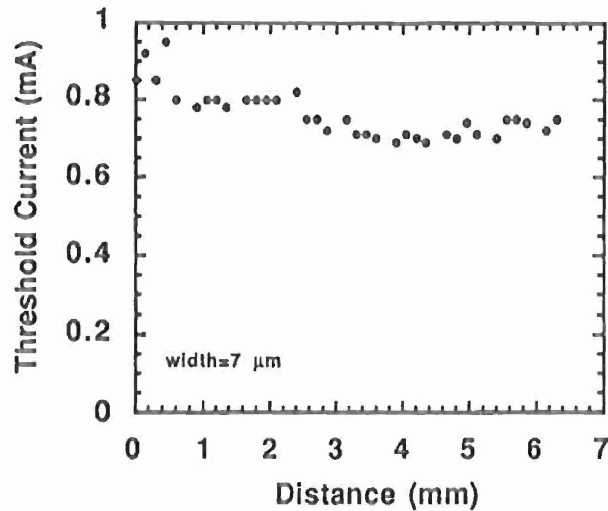


Figure VII. 6. Threshold current vs distance.

linewidth the spectral linewidth of a 12 μm device was measured by using an interferometric fringe visibility technique. The laser output was collimated into a 1.5 cm diameter beam using a single lens and was directed into a free-space Mach-Zehnder interferometer in which the length of one

path could be changed. The interferometer output was cycled through constructive and destructive interference by modulating the position of one mirror several $1/2$ wavelengths with a piezoelectric translator. A detector at the output was used to measure the resulting modulation. By varying the delay τ and measuring the modulation depth, m , the coherence time, τ_c , was determined from the exponential decay of the modulation depth with increased delay; i.e. $m \propto \exp(-\tau/\tau_c)$. The corresponding linewidth as a function of output power is plotted in Figure VII. 7. The minimum linewidth is 85 MHz at 60 μW output power with a linewidth-power product of 5 MHz $\cdot\text{mW}$. This is the lowest linewidth-power product ever reported for a VCSEL[18], and it is comparable to the best in-plane lasers.

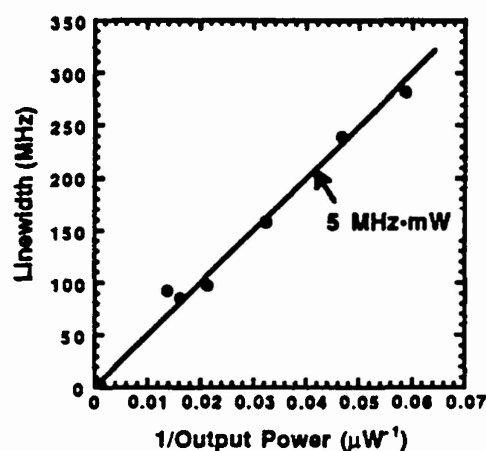


Figure VII. 7. VCSEL Linewidth.

VIII. THEORETICAL GAIN IN STRAINED AND UNSTRAINED QUANTUM-WELL LASERS

A. Introduction

The rapid progress in the fabrication of viable VCSELs, which utilize strained InGaAs/GaAs quantum wells, has provided a strong motivation for developing a theory which gives an accurate description of the optical gain properties of strained InGaAs quantum wells. Armed with the knowledge of how the optical gain behaves as a function of injected current density, we can hope to optimize the design of surface-emitters such that external quantum efficiency can be maximized, and hence, the current required to obtain a given amount of output power can be minimized.

Calculation of the gain in quantum wells is complicated by the fact that the valence band structure is very complex, due to the interaction between heavy and light hole bands, which occurs whenever there is quantum confinement. This phenomenon is known as valence band-mixing, and it tends to distort the parabolic bands into warped complex curves (as we will discuss in more detail below). This warping behavior has a detrimental effect on the gain properties of the quantum well. Recently, it has been suggested that compressive strain introduced into quantum wells should help alleviate this problem [19, 20], and at the same time reduce the effective mass in the heavy hole band, both of which should increase the efficiency of producing optical gain in the material.

Over the past year, we have made a serious effort to perform detailed calculations of valence band-mixing effects and the resulting gain characteristics of strained and unstrained quantum wells. A detailed computer program has been developed which has the capability to analyze and predict various properties of quantum wells such as the valence subband structure, the optical gain spectrum, the spontaneous emission spectrum, the peak gain (and the gain at a particular wavelength) as a function of carrier density and radiative current density, as well as other features. The program has been applied to strained and unstrained GaAs and InP based material systems, and is easily extendible to other material systems. Our efforts have resulted in the

publication of two journal papers [15, 4] and we have also written a book chapter [22] which goes into the fundamentals of the theory of optical gain in semiconductors, and explains in some detail the methods we have used to calculate the band structure and material gain. In what follows, we will describe in more detail the work we have done in both GaAs and InP material systems.

B. Calculations

In the GaAs system, we have performed a detailed analysis of strained $\text{In}_x\text{Ga}_{1-x}\text{As}/\text{Al}_{0.2}\text{Ga}_{0.8}\text{As}$ 80Å quantum wells [15], concentrating on how the gain characteristics are modified by the addition of varying amounts of strain (amount of indium) in the well. The specific well width and material parameters were chosen to coincide with the active regions we currently employ in our sub-milliwatt strained InGaAs Surface-Emitting Lasers. The results of the valence subband structure calculations are shown in Figure VIII. 1 for (A) an unstrained GaAs/ $\text{Al}_{0.2}\text{Ga}_{0.8}\text{As}$ 80Å quantum well, and (B) a strained $\text{In}_{0.2}\text{Ga}_{0.8}\text{As}/\text{Al}_{0.2}\text{Ga}_{0.8}\text{As}$ 80Å quantum well. In case (A), the dramatic non-parabolicity observed in the subband structure is a direct result of the band-mixing between the HH and LH subbands. In case (B), the strain separates the HH and LH subbands, pushing the LH subbands further into the well (they cannot even be seen in the energy range appearing in the graph). As a result, the band-mixing effects are greatly reduced, leading to a much 'lighter' subband structure in the strained case. This is perhaps more easily observed by comparing the density of states (DOS) in the two cases, shown at the right of each plot (the valence band DOS curves are plotted relative to the constant DOS of the first conduction subband). In the ideal case, we would like $p_v/p_c = 1$. Thus, the DOS plots dramatically illustrate how strain can help optimize the subband structure.

The results of the gain calculations are shown in Figure VIII. 2 for the two structures illustrated in Figure VIII. 1. For comparison purposes, we have included a simplified parabolic band model (dashed curves) for both the strained and unstrained quantum wells, using the bulk parabolic valence band strained and (100) unstrained effective masses. Features of Figure VIII. 2 that are of practical interest include: (1) the current or carrier density required to reach zero loss and

gain in the material, the so-called transparency level, n_{tr} and J_{tr} , and (2) the differential gain which is the rate of increase in the gain as a function of carrier or current density. The advantages of the strained quantum well are clearly evident from Figure VIII. 2, where both a lower transparency level and a higher differential gain are simultaneously achieved. This is again mainly due to the close match in the conduction and valence band density of states.

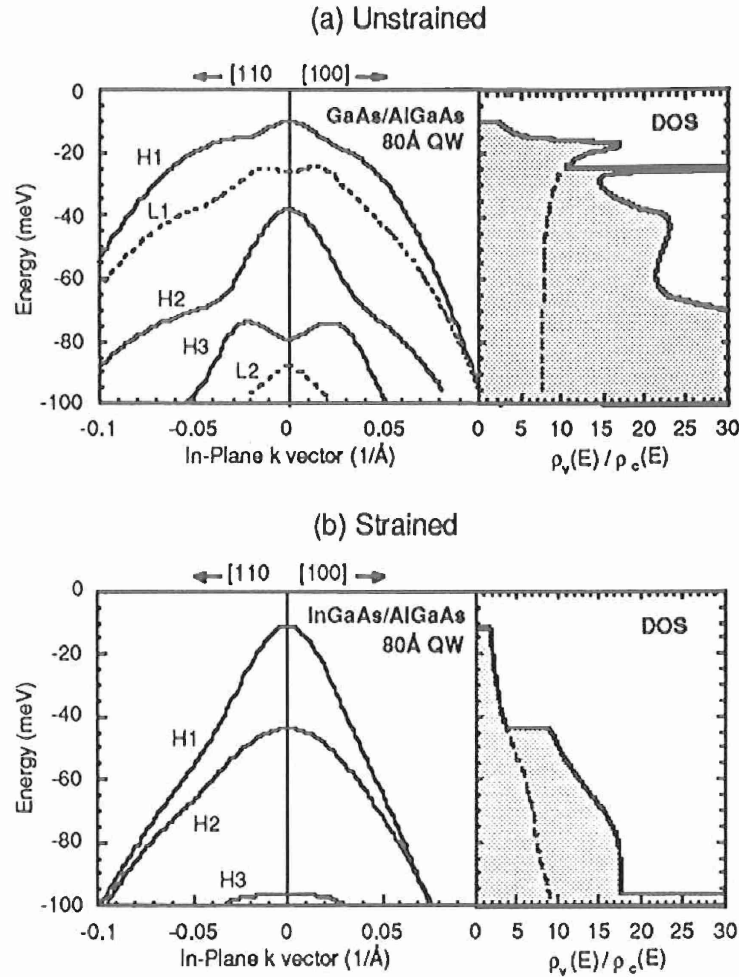


Figure VIII. 1. Valence subband structure of (a) an 80Å GaAs/Al_{0.2}Ga_{0.8}As quantum well ($V_0 \approx 95$ meV), and (b) an 80Å In_{0.2}Ga_{0.8}As/Al_{0.2}Ga_{0.8}As strained quantum well ($V_0 \approx 175$ meV). The coupling between the HH (solid curves) and LH (dashed curves) subbands is very dramatic in the unstrained case (a). Note that the [110] and [100] dispersion characteristics are slightly different, with a 'heavier' band structure observed along the [110] direction. At right is the total (solid curve) and H1 subband (dashed curve) density of states plotted relative to the density of states in the first conduction (C1) subband. The zero slope in the L1 subband away from $k = 0$ is seen to result in a pole in the DOS of case (a).

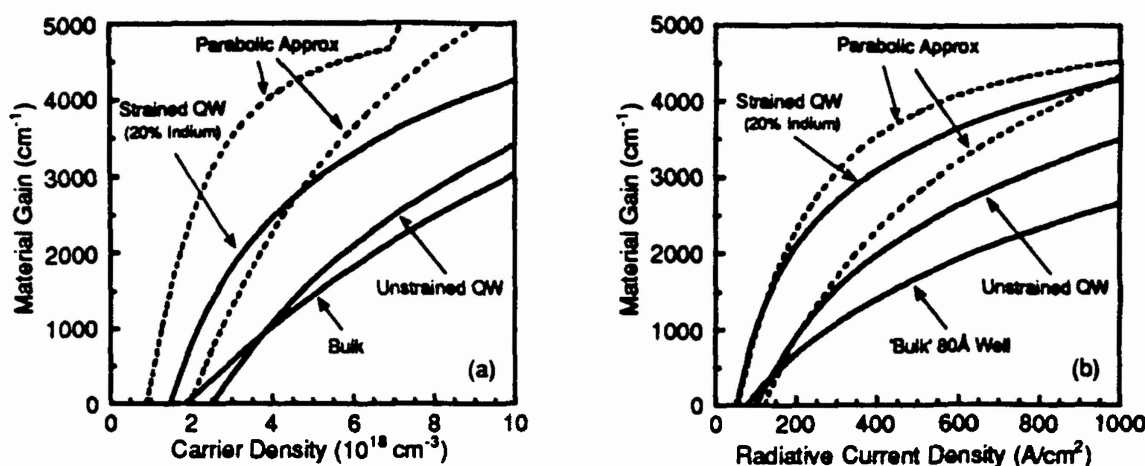


Figure VIII. 2. Comparison of the peak material transverse electric (TE) gain as a function of (a) carrier density, and (b) radiative current density. Auger recombination and other non-radiative mechanisms have not been included, thus, the material gain as a function of *total* current density is expected to be suppressed by 10-30% of that shown, under high injection conditions.

The parabolic band models have been included to emphasize the necessity of including valence band-mixing effects when calculating material gain. The *relative* benefits of moving to a strained quantum well predicted with the parabolic band model are in qualitative agreement with the more detailed calculations. However, in general, the parabolic band model produces numbers which are overly optimistic. For example, the parabolic model dramatically underestimates the carrier density required to achieve a given gain in both strained and unstrained cases. The literature is filled with parabolic band models; however, as Figure VIII. 2 reveals, the more detailed calculation which includes the band-warping illustrated in Figure VIII. 1 does have a substantial effect on the predicted gain behavior and should not be neglected. In addition, the parabolic band models cannot be used to predict the gain behavior as a function of increasing strain (in a parabolic band model, strain is either on or off, there is no in-between). The band-mixing model naturally includes the degree of strain which is applied.

As an example, we show in Figure VIII. 3 relevant gain characteristics of a strained $\text{In}_x\text{Ga}_{1-x}\text{As}/\text{Al}_{0.2}\text{Ga}_{0.8}\text{As}$ 80Å quantum well as a function of the indium mole fraction in the well using valence subband structures similar to those calculated in Figure VIII. 1. As can be seen, the

gain characteristics dramatically improve as more strain is added to the well. Figure VIII. 3 suggests that transparency current densities should be reduced by a factor of two (from 100 to 50 A/cm^2) simply by moving from a GaAs quantum well to an $\text{In}_{0.2}\text{Ga}_{0.8}\text{As}$ quantum well. This translates into similar reductions in the threshold current of a semiconductor laser. The transparency carrier density is also reduced from 2.5 to $1.5 \times 10^{18} \text{ cm}^{-3}$. The differential gain is predicted to be enhanced by a factor of two, which translates into a factor of $\sqrt{2}$ enhancement in the modulation speed of the laser. By increasing the indium mole fraction from 20% to 50%, our theoretical model suggests that transparency current densities should drop below $40 \text{ A}/\text{cm}^2$ and that transparency carrier densities should approach $1 \times 10^{18} \text{ cm}^{-3}$. Thus, in the GaAs system, tremendous potential benefits arise from the addition of compressive strain into a quantum well.

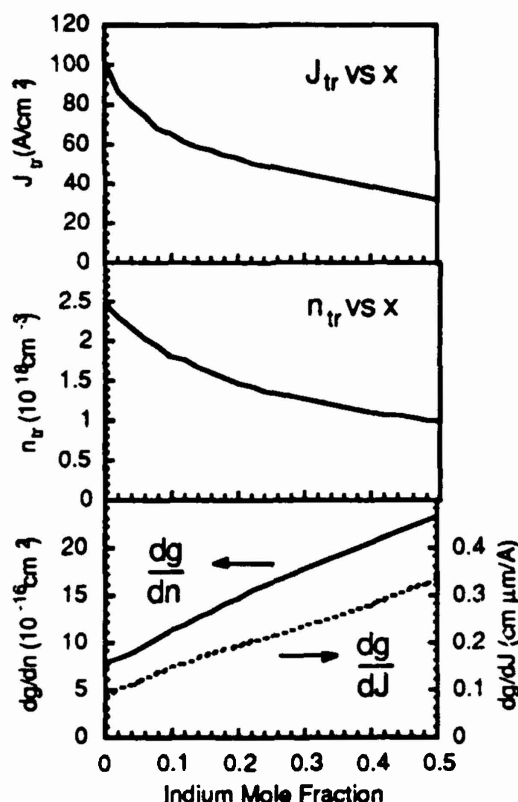


Figure VIII. 3. Gain characteristics of a strained 80\AA $\text{In}_x\text{Ga}_{1-x}\text{As}/\text{Al}_{0.2}\text{Ga}_{0.8}\text{As}$ quantum well as a function of indium mole fraction, x . (The differential gain, dg/dJ , has been multiplied by the well width of 80\AA to obtain units of $\text{cm } \mu\text{m}/\text{A}$).

Compressive strain has been considered as having an even greater impact in the longer wavelength InP material system. This is largely due to the fact that in these lower band gap materials, a significant fraction of the total threshold current consists of detrimental non-radiative Auger recombination current (which increases in proportion to n^3). For example, if compressive strain could be used to reduce the threshold carrier density by a factor of two, the corresponding Auger current could be reduced by a factor of eight! Hence, it would be very useful to know how strain affects the threshold carrier density of InP lasers.

As an example, we chose to study a 40 Å quantum well grown on a (100) InP substrate [23]. The well material used in our calculations was $\text{In}_x\text{Ga}_{1-x}\text{As}$, which in the InP system can result in either compressive or tensile strain depending on whether $x > 0.53$ or $x < 0.53$, resp. The quaternary $\text{In}_{0.86}\text{Ga}_{0.14}\text{As}_{0.3}\text{P}_{0.7}$ (with 1.083 μm band gap and lattice-matched to InP) was chosen as the barrier material to ensure that the conduction band barrier height would remain larger than 100 meV. The results of the subband structure calculations are shown in Figure VIII. 4 for: a) compressive strain with $x_{\text{ind}} = 0.68$ ($\lambda_{\text{C1-HH1}} = 1.604 \mu\text{m}$), b) no strain with $x_{\text{ind}} = 0.5321$ ($\lambda_{\text{C1-HH1}} = 1.429 \mu\text{m}$), and c) tensile strain with $x_{\text{ind}} = 0.38$ ($\lambda_{\text{C1-HH1}} = 1.283 \mu\text{m}$).

The main effect of the strain is to change the relative placement of the light hole (LH) subband within the quantum well. For example, in Figure VIII. 4a where there is appreciable compressive strain, the LH subband is quite removed from the two lowest heavy hole (HH) subbands. The result is a fairly parabolic subband near the band edge with "light hole character" extending ~ 40 meV into the band. In Figure VIII. 4b where no strain is applied, the LH subband moves up between the two HH subbands, repelling the HH subbands away from it. The result is a much "heavier" band structure near the band edge. For the tensile strain case shown in Figure VIII. 4c, the LH subband moves up enough to actually become the lowest subband in the well. And while the HH and LH subbands are close to degenerate at the zone center, they quickly separate as soon as they gain some in-plane momentum. The result is a band structure with an inverted curvature at the zone center. The undesirable consequence of this is that as we inject current, the holes will initially populate regions *away* from the zone center, making it that much

more difficult to create a "population" or more correctly, an "occupation probability" inversion at the zone center. Thus, the general trend observed in Figure VIII. 4 is that the further removed the LH subband is from the lowest HH subband, the less band-warping there is, and the "lighter" the overall band structure becomes. It is this "light hole character" which improves the gain characteristics of the material; and hence, we should expect that compressive strain holds the most promise.

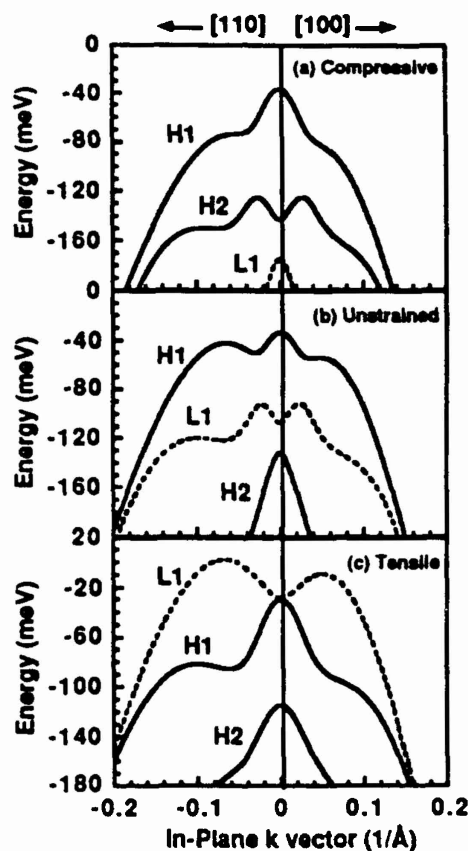


Figure VIII. 4. Valence subband structure of a 40 Å $\text{In}_x\text{Ga}_{1-x}\text{As}/\text{In}_{0.86}\text{Ga}_{0.14}\text{As}_{0.3}\text{P}_{0.7}$ quantum well for (a) compressive strain with $x_{\text{ind}} = 0.68$ ($\lambda_{\text{C1-HH1}} = 1.604 \mu\text{m}$), (b) no strain with $x_{\text{ind}} = 0.5321$ ($\lambda_{\text{C1-HH1}} = 1.429 \mu\text{m}$), and (c) tensile strain with $x_{\text{ind}} = 0.38$ ($\lambda_{\text{C1-HH1}} = 1.283 \mu\text{m}$). The bulk strained band gaps in the well for the three a, b, c cases are: $E_g(\text{HH}) = 635, 748, 869 \text{ meV}$, and $E_g(\text{LH}) = 699, 748, 790 \text{ meV}$, resp. The zeros of the energy scales on the vertical axis correspond to the heavy hole material band edge in each case. Note that the [110] and [100] dispersion characteristics are slightly different, with a 'heavier' band structure consistently observed along the [110] direction.

Figures VIII. 5a-b show the results of our gain calculations for the three indium compositions mentioned above and in Figure VIII. 4. In Figure VIII. 5a, the transverse electric (TE) peak gain (which corresponds to the gain seen by an optical field with its electric field polarized in the plane of the well) reveals dramatic differences between the three cases, with compressive strain ($x_{\text{ind}} = 0.68$) exhibiting the best performance. Figure VIII. 5b displays the transverse magnetic (TM) peak gain (where the electric field is polarized perpendicular to the plane of the well). We see that the trend is reversed in this case, with the tensile strain ($x_{\text{ind}} = 0.38$) producing the most gain. Comparing the TE gain to the TM gain directly for a given indium mole fraction, we find that for the unstrained and compressively strained cases, the TE gain performs much better. However, for $x_{\text{ind}} = 0.38$, the TM gain actually dominates, implying that tensile strained lasers should lase preferentially in the TM mode (provided enough tensile strain is "designed" into the quantum well).

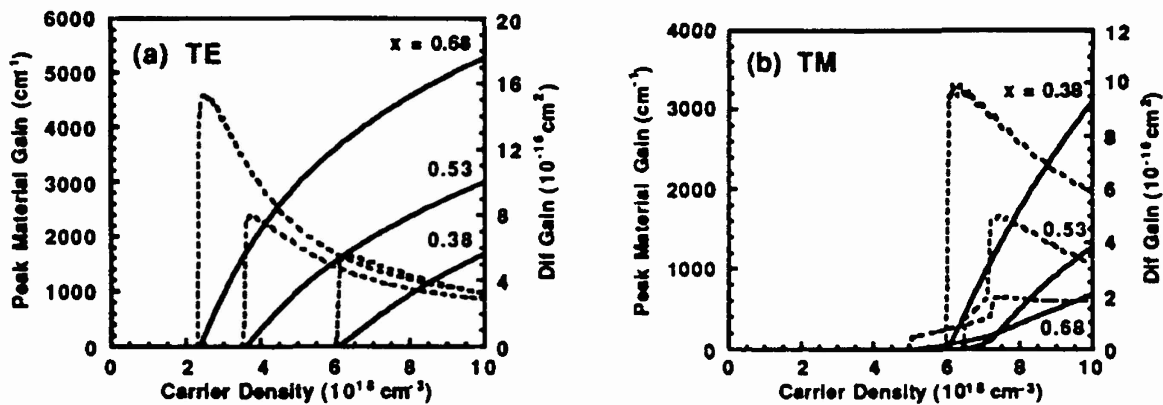


Figure VIII. 5. Peak material gain (solid curves) and the derivative of the peak gain, or differential gain (dashed curves) plotted as a function of carrier density for (a) TE optical modes and (b) TM optical modes. The gain as a function of the sheet carrier density (cm^{-2}) is obtained by multiplying the x-axis by $40 \times 10^{-8} \text{ cm}$.

We have so far discussed the gain characteristics for three discrete indium mole fractions. The trends discussed above are perhaps more easily observed as a continuous function of indium composition in the well. In Figure VIII. 6 we plot the transparency carrier density and

transparency differential gain as a function of indium mole fraction in the well for both TE and TM gain. We also include the wavelength at which the peak gain occurs. Again we find that compressive strain reduces the carrier density needed to reach transparency in the material, which should lead to correspondingly lower Auger currents. From Figure VIII. 6, it would appear that the more compressive strain, the better. However, in practice, growth constraints and critical thickness limitations will ultimately determine how much strain can be tolerated.

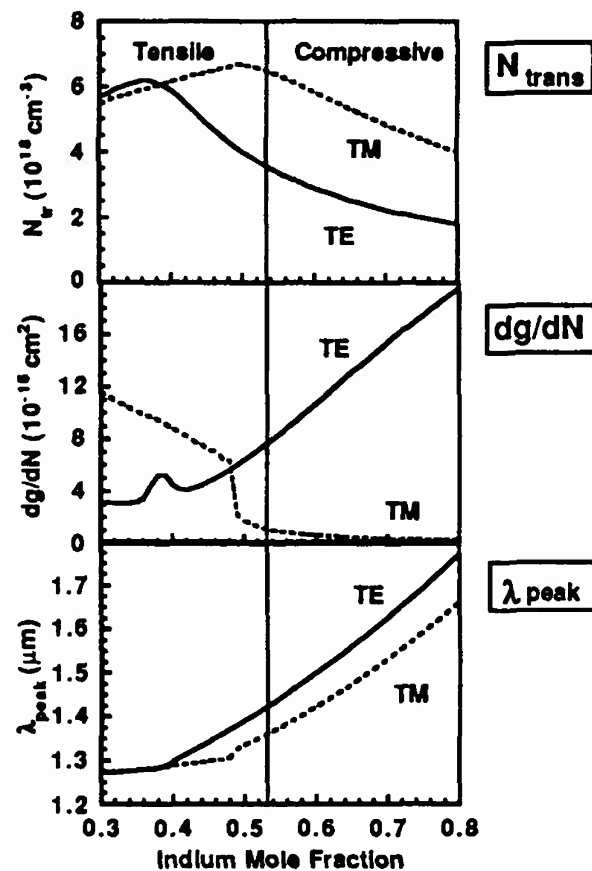


Figure VIII. 6. Transparency carrier density, differential gain, and corresponding transition wavelength of a strained 40 Å $\text{In}_x\text{Ga}_{1-x}\text{As}/\text{In}_{0.86}\text{Ga}_{0.14}\text{As}_{0.3}\text{P}_{0.7}$ quantum well as a continuous function of indium mole fraction, x , in the well, for both TE and TM optical modes.

We are at a stage now where we feel that we can predict how the optical gain behaves as a function of injected current density reasonably well. The next step is then to apply these relationships to practical device designs. Figure VIII. 7 which is taken from Ref.[14] shows

typical design curves we have generated for strained InGaAs quantum well SEL's using the theoretical gain vs current relationships discussed above. Also shown are experimentally measured threshold currents of real SEL devices as discussed in detail in Ref.[23]. The agreement is reasonable, which encourages us to believe what the design curves suggest as the optimum cavity designs. For example, single quantum well active region SEL's initially demonstrated low thresholds, but the external efficiencies were very low. As a result, not much output power could be obtained. Thus, it was necessary to reduce the mirror reflectivity to improve the output coupling. Using the theoretical design curves as a guide, we have been able to determine the best compromise between reducing the mirror reflectivity to get more power out, and keeping the gain per quantum well low enough that reasonable threshold currents can still be obtained. At present we are experimenting with three quantum well active region devices, which from initial indications, appear to be yielding relatively large external efficiencies ($>40\%$ on broad area devices) while maintaining low threshold current densities ($>1 \text{ kA/cm}^2$).

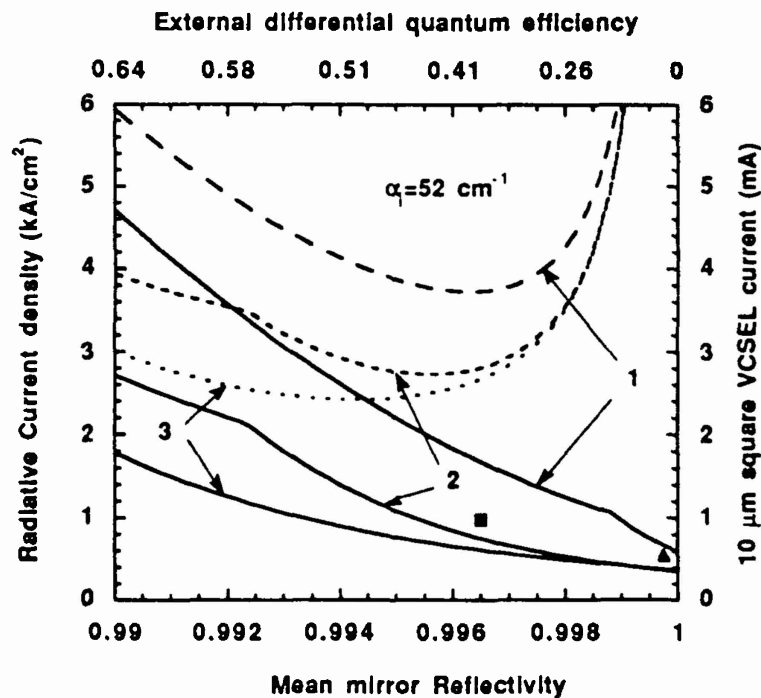


Figure VIII. 7. Current density needed to reach threshold (solid lines) and 1 kW/cm^2 ($1 \text{ mW}/100 \mu\text{m}^2$) output power (dotted lines) for 1, 2, and 3 quantum wells. The onset of the $n=2$ transition can be seen at $R=0.999$ for one quantum well and $R=0.9925$ for two. An internal loss of 52 cm^{-1} is assumed. Data points are for actual VCSELs with one quantum well (triangle) and two quantum wells (square).

Thus, our efforts to calculate the optical gain in quantum wells more accurately by including the effects of valence band-mixing have been beneficial in many ways. The effects of strain on the gain behavior of quantum wells have been elucidated in both of the primary material systems of interest for opto-electronic applications. The results of the gain calculations have been successfully applied to the design of SEL's. In addition, the formalism used here to determine the valence subband structure in quantum wells is at present being extended (by Yi???) to the analysis of structures which provide quantum confinement in more than one-dimension (so-called quantum wires).

IX. References

- [1] T. Egeler, G. Abstreiter, G. Weimann, T. Demel, D. Heitmann, P. Grambow, and W. Schlapp, *Phys. Rev. Lett.*, **65**, 1805 (1990).
- [2] Kapon et al., *Phys. Rev. Lett.*, **63**, 430, (1989).
- [3] J. M. Gaines, et al., *J. Vac. Sci. Technol., B* **6**, 1378 (1988).
- [4] M. S. Miller, et al., *Seventh International Conference on Integrated Optics and Optical Fiber Communication, Paper ThP-45*, Athens, Greece (1990)
- [5] J.A. Skidmore, et al., *3 Beams Conf.*, Seattle, WA, (May, 1991).
- [6] M. Cao, et al., *Integrated Optics and Optical Fiber Communication*, Technical Digest, 20PDB-10 (1989).
- [7] Y. Arakawa and A. Yariv, *IEEE J. Quantum Electron.*, **QE-22**, 1887 (1986).
- [8] M. Tsuchiya, L. A. Coldren, and P. M. Petroff, *Integrated Optics and Optical Fiber Communication*, Technical Digest, 19C1-1 (1989).
- [9] J. C. Yi, N. Dagli, L. A. Coldren, *Quantum Optoelectronics*, Technical Digest Series 7, 12 (1991).
- [10] J.C. Yi, N. Dagli, L.A. Coldren, *Appl. Phys. Lett.*, **59**, (July, 1991).
- [11] K. Kojima, K. Mitsunaga, and K. Kyuma, *Appl. Phys. Lett.*, **55**, 882, (1989).
- [12] H. Weman, M. S. Miller, P. M. Petroff, H. Kroemer and J. L. Merz, *Bull. Am. Phys. Soc.*, **36**, 824 (1991).
- [13] M. Tsuchiya, J. M. Gaines, R. H. Yan, R. J. Simes, P. O. Holtz, L. A. Coldren, and P. M. Petroff, *Phys. Rev. Lett.*, **62**, 446 (1989).

- [14] E. Marclay, D.J. Arent, C. harder, H.P. Meier, W. Walter and D.J. WEbb, *Electronics Letters*, **25**, N14, 892-894, (July 6, 1989).
- [15] S.W. Corzine, R.H. Yan and L.A. Coldren, *Appl. Phys. Ltrs.*, **57**, (26) 2835-2837, (December 24, 1990).
- [16] R. Geels, R.H. Yan, J.W. Scott, S.W. Corzine, R.J. Simes, and L.A. Coldren, *Proc. CLEO'88*, Anaheim, CA, paper WM1. (1988).
- [17] R.S. Geels, S.W. Corzine, J.W. Scott, D.B. Young, and L.A. Coldren. *IEEE Photon. Technol. Lett.*, **2**, 234 (1990).
- [18] R.S. Geels, and L.A. Coldren, *Appl. Physics Letts.*, **57**, (October 15, 1990).
- [19] A.R.Adams, *Electron. Lett.* **22**, 249 (1986).
- [20] E.Yablanovitch and E.O.Kane, *IEEE J. Lightwave Technol.* **LT-4**, 504 (1986).
- [21] S.W. Corzine and L.A. Coldren, *Appl. Phys. Lett.*, **59**, (July 1991 Issue).
- [22] S.W. Corzine, R.H. Yan, and L.A. Coldren, *Quantum Well Lasers*, Chapter 1, Editor P.Zory, Academic Press, to be published in early 1992.
- [23] R.S. Geels, S.W. Corzine and L.A. Coldren, to be published in *IEEE J. Quantum Electron.* (June 1991 Issue, **QE-27**).

X. Scientific Personnel

1. Larry A. Coldren: Principal Investigator
2. J.L. Merz: Associate Investigator
3. A.C. Gossard: Associate Investigator
4. N. Dagli: Faculty Collaborator
5. J.H. English: Development Engineer
6. D.A. Cohen: Development Engineer
7. S.W. Corzine: Student
8. D.B. Young: Student
9. J.C. Yi: Student
10. S.-Y. Hu: Student